CFD-MODELLING AND THERMAL CHARACTERIZATION OF FRICTION STIR WELDING USING TOOL WITH POLYGONAL PINS

Esam Hamza

Libyan Authority for Scientific Research, Tripoli, Libya
E-Mail: esam.hamza@lwc.ly

الملخص.

خلال العقدين الماضيين، أظهر اللحام الاحتكاكي العجائني FSW القدرة على إنتاج وصلات ذات مقاومة عالية خصوصا للمواد التي يتعذر لحامها بواسطة عمليات اللحام التقليدية. لذلك، فإن تحسين جودة الوصلات الملحومة بتحديد أفضل متغيرات لهذه العملية لايزال موضوع بحث مهم. في ضوء ذلك، قد يؤدي التحكم الفعال في الدورة الحرارية لعملية اللحام هذه ومن خلال المتغيرات التشغيلية والشكلية إلى تجنب العيوب التي قد تحدث في الوصلة. العديد من الدراسات أجريت باعتبار أشكال مختلفة لرأس أداة اللحام وذلك لتحسين الخواص الميكانيكية للوصلة الملحومة، غير أن تأثيره وبشكله المضلع على الخصائص الحرارية للقطعة الملحومة لم يحظى إلا بقدر بسيط من الإهتمام. إلى جانب ذلك، أبدى العمل التجريبي في كثير من الأحيان أنه مكلف ويستغرق وقتاً طويلاً خاصة عند دراسة تأثير المتغيرات المتعلقة بشكل أداة اللحام. تركز هذه الدراسة على التوظيف التكاملي للمنهج التحليلي وكذلك أدوات ديناميكيات الموائع الحسابية CFD في محاكاة التوليد الحراري والحقل الحراري المصاحب لعملية اللحام وذلك عند استخدام رؤوس مضلعة الشكل. تم استخدام نموذج عددي معدل CFD ثلاثي الابعاد يعتمد على كل من الشبكة الديناميكية والشبكة المنزلقة وذلك للتحقق من تأثير نطاق واسع من المتغيرات التشغيلية والشكلية على التوزيع الحراري ودرجة حرارة الذروة في الملحومات السميكة. أيضاً تم تطوير مجموعة من الصيغ التحليلية لحساب كمية التوليد الحراري لأي تغيير في شكل رأس أداة اللحام. إستطاع النموذج المحسن تحديد التوزيع المكاني والزمني لدرجة الحرارة في جميع عمليات اللحام وكذلك حساب كمية المعدن السائل المتكونة عندما تتجاوز درجة حرارة المادة درجة حرارة تصلبها. علاوة على ذلك، أستخدمت النتائج العددية المتحصل عليها في تطوير نموذج شبه تجريبي لحساب درجة حرارة الذروة.

ABSTRACT

In the last two decades, Friction Stir Welding (FSW) has shown a capability to produce high strength joints particularly for the materials that cannot be welded by the conventional welding processes. Hence, optimizing the FSW process parameters to improve the quality of welded joint is still a subject of active research. In view of that, the efficient control of the welding thermal cycle through the geometrical and operational parameters may lead to produce sound weldments where defects can be avoided. Various studies have been carried out considering different tool pin profiles to improve the mechanical strength of welded joint, but the influences of the polygonal pin profiles on the thermal characterizations have been rarely reported in details. Besides, the experimental work has often showed that it is cost and time consuming particularly when the effect of geometrical variables is investigated. The present work focuses on the integral employment of analytical approaches and Computational Fluid Dynamics (CFD) tool to simulate the heat generation and the thermal field associated to the FSW when using tool with polygonal pins. A three-dimensional CFD model considering both dynamic mesh and sliding mesh techniques has been used to investigate the effect of a wide range of geometrical and operational parameters on the temperature distribution and peak temperature within thick FS welded workpieces. A set of novel analytical

formulas have been developed to calculate the amount of heat generation corresponding to the pin shape. The improved numerical model has captured the temporal and spatial temperature distribution throughout the weldments and succeeded to monitor the liquid fraction when the material temperature exceeding the solidus temperature. Moreover, the acquired numerical results have then been used to develop a novel semi-empirical prediction model for the peak temperature.

KEYWORDS: Friction Stir Welding (FSW); Polygonal Pin; Analytical Approaches; Computational Fluid Dynamics (CFD); Dynamic Mesh; Liquid Fraction.

INTRODUCTION

Although, friction stir welding is relatively new process compared to the conventional welding processes it has experienced a rapid utilization in a wide variety of industries such as aerospace, automotive and naval applications [1]. This welding process has helped to achieve high quality welded joints which overcomes many of the problems associated with traditional joining techniques. The welding temperature in FSW does not advantageously exceed the melting point, filler metals and shielding gases are not required. Furthermore, it is an effective alternative to weld dissimilar materials. In FSW process a non-consumable rotary tool consisting of shoulder and a pin is brought in between the adjacent plates needed to be welded. This stage is called plunging, where the tool penetrates gradually in the workpiece due to the axial load applied by the machine. Then, dwelling stage in which the tool keeps rotating in the same position where the heat that is generated due to frictional activities and plastic deformation leads to increase the temperature of the surfaces being welded in the near-tool region and makes them soft. After that the tool is forced to move along the joint line in the welding stage with high mechanical pressure that melds and joins both materials together [2].

It is well established in friction stir welding those parameters such as rotational speed, translational speed, and the tool geometry control the character of the weld. These parameters determine the amount of energy input to the weld and the rate of heat generation at the tool/material interface. Hence, peak joint temperature and temperature profile in the region near the joint can have a significant impact on the plastic deformation zone and heat affected zones, as well as the joint properties. The tool geometry is determined by geometrical aspects related to dimensions and shapes of both the pin and the shoulder. The pin shape is no less important than the shoulder where when it comes to welding of thin plates, the shoulder surface has the major part in generation of heat by friction whereas in thicker plates; the pin role becomes more efficient at the same time [3]. Therefore, proper pin design can lead to an effective FSW process which also means broadening the process's applicability. Although, various studies have been carried out considering different tool pin profiles to improve the mechanical strength of welded joint, but the influences of the pin shape on the thermal aspects have been rarely reported [4,5]. Regardless of the features on the pin side face, circular sided pin is used to some extent. However, polygonal pin can enhance the mechanical strength of the joint which might be attributed to the change in the thermal performance that can impact the grain size and the final weld microstructure [6]. In the following section a review of important research works carried out regarding using tool with polygonal pins.

Friction stir welding using tool with polygonal pins

Fujii et al. [7] published a research study in which 5mm thick sheets of Aluminium were friction stir welded to investigate the effect of the tool shape on the mechanical properties and the microstructure. Additionally, two welding tools with threaded and non-threaded cylindrical pins were used as well as one more with triangular pin profile. This study has revealed that for Aluminium alloys that have a relatively high resistance of deformation, the triangular prism pin has given the best results particularly at high rotational speeds. However, a limited pin shapes have been included in the study and no detailed information regarding the thermal behavior within the workpiece has been presented. Elangovan et al. [8-10] conducted a series of experimental studies to comprehend the effects of operational and geometrical parameters on friction stir welded zone formation. To this end, authors employed different rotational speeds, axial forces, shoulder diameters and five pin profiles including triangle and square shapes in joining of two Aluminium plates with a thickness of 6mm. In all studies, the results have shown that the optimum mechanical properties and free defect welds have been produced by using the tool with a square pin. The same finding has been achieved when Gharaibeh et al. [11] carried out similar investigation by considering triangular, square and hexagonal pins. Irrespective of the achievements, more comprehensive analysis could be conducted using a wider range of process geometrical and operational parameters particularly on the thermal impacts that have a significant role in the zone formation. Biswas et al. [12] carried out a research work in which 6mm of a commercial grade Aluminium was friction stir welded in order to experimentally detect the effects of the pin profile, rotational and translational speed on the mechanical properties and microstructural features of the welded joints. Five various pin profiles including the hexagonal profile have been considered. Vijay et al. [13] have experimentally investigated the effects of the change in polygonal pin shape on microstructure and tensile strength while friction stir welding of 6mm thickness of ceramic matrix composites. In view of the number of pin side faces, polygonal pins with 4, 6 and 8 faces were employed. The study concluded that the tensile strength and the microstructure of the welded joint are affected by the change in the polygonal pin profile. In order to develop a mathematical model predicting the ultimate tensile strength, Gopalakrishnan [14] has only considered square and hexagonal tool pins with different operational conditions. In doing so, friction stir welds were made for plates of square butt joint. The model revealed that the tool pin profile and the welding speed recorded the highest effects on the tensile strength. Further experimental studies were carried out by Palanivel et al. [15] Vijayan et al. [16] to examine how the pin profiles in FSW of dissimilar Aluminium alloys affect the tensile properties of welds along with other process parameters. Mehta et al. [5] carried out an investigation on the adhesion of plasticized material on pin surface. Because of the very high values of stresses that are achieved when using the polygonal pins, the authors presumed various polygonal pins (triangle, square, pentagon, hexagon, and cylindrical) and welding parameters in the study to analyze the extent of undesirable adhesion which would lead to lose the pin functionality. The results showed that the pins having less than six sides recorded the optimum reaction to the adhesion. The effects of pin profiles on the superplastic behaviour have also been investigated by Pate et al. [17] who used square, pentagon and hexagon pins. Recently, Mugada analyzed the material flow experimentally using a marker insert technique during FSW with different polygonal pins. [18]

For difficulties of estimating of process thermal features and to overcome the

problem of the high cost and time consuming of the experimental investigations related to the tool geometry, researchers have used both numerical and analytical approaches as alternatives. Accordingly, Finite Element Method (FEM) has been used by Buffa et al. [19] where tapered and cylindrical pins used to study the influence of the tool angle on the zones of welded joint. Jaimin and Patil [20] and Marzbanrad et al. [21] have also considered FEM to investigate the mechanical properties and thermal analysis. Very limited types of polygonal pins were employed among different pin profiles used.

As a powerful modelling tool, CFD based thermal and material flow studies [22-39] have been published. Noticeably, limited studies have investigated the effect of polygonal pin profile on the thermal field where detailed information about the spatial and transient thermal features was rarely reported.

Gadakh et al. [40] proposed analytical models to estimate the frictional heat generation for tools with different pin shapes including triangular, square, pentagon and hexagon. However, this study could be expanded by covering more polygonal pins.

Based on the above presented literature review, it can be summarized that the FSW tool pin designing is still a field of research as more possibilities of polygonal pin profiles can be considered. The published literature is also severely limited in terms of the thermal field analysis within the workpiece particularly the thicker ones. In the view of modeling, it is decisively needed to estimate the heat generation amount. From another point of view, there is a lack in the relationships for the process thermal aspects that include both the geometrical and operational parameters. Therefore, the present work focusses on the thermal field diagnostics of FSW using tools with different polygonal pins where CFD tools with advanced modelling techniques are suggested to be used for analysis of the thermal field. To accomplish the modelling process, a customised analytical approach will be demonstrated to determine the value of heat generation for all proposed tools with polygonal pins. Furthermore, detailed numerical investigations will be carried out for analyzing the effects of a wide range of geometric and operational parameters on the thermal field within the workpiece. Lastly, based on the investigation conducted, a semi-empirical prediction model for the peak temperature has been developed.

CFD MODELLING OF FRICTION STIR WELDING

The current numerical model is an improved version of the model that was developed by Hamza et al [41-42] where, a new methodology proposed to avoid the unnecessary assumptions and getting more realistic model as well as enhancing the model capability in terms of computation time. For this purpose, solidification/melting model and special setting for dynamic mesh have been considered. ANSYS Fluent 17.0 has been used in the development of the current numerical model, which is three dimensional, transient and based on a very limited fluid region. The next section provides detailed information regarding the CFD setup that has been used in the present study.

Model regions and geometry

Using the Design Modeller facility in ANSYS 17.0, the geometric details of the model have been created. As it can be seen in Figure (1), the current numerical model has two main regions; the first one represents the thermomechanical affected zone (TMAZ) around the tool. This zone is treated as a fluid region which has a conical shape where, its dimensions are estimated based on design variables "x_1" and "x_2" as displayed in Figure (2). According to Kang et al. [37] and Hamza et al [41-42], the

dimensions of this rotational zone "x_1" and "x_2" are 1mm and 2.5mm, respectively. The second region represents the other part of the workpiece which is treated as a solid region. Based on practical dimensions from the literature [43], the numerical model of the computational domain consists of volumes of two plates of aluminium alloy AA6061, in contact with each other. The tool, consisting of the shoulder and the pin is inserted into the workpiece at the interface of the two plates. The tool pin has a cylindrical profile with a radius of 6 mm and a length of 12.0 mm, where the shoulder has a constant radius of 25mm. The tool was simulated as a wall after cutting its material volume from the workpiece. The dimensions of each plate to be welded are 254 mm x 102 mm x 12.7 mm.

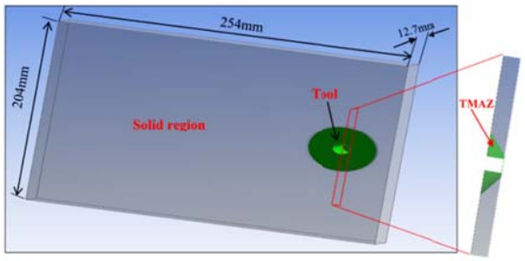

Figure 1: The main regions in the computation domain

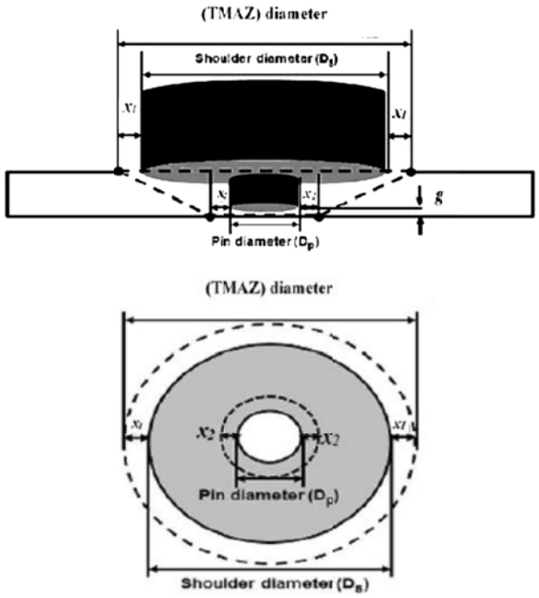

Figure 2: Thermo-mechanical affected zone details [37]

Meshing of the computational domain

The mesh quality and providing the minimum number of elements have been carefully considered during the mesh generation process. Moreover, looking at the objectives of the current study which aim to achieve a more realistic model, the tool motion has also considered in estimation of the meshing techniques. Accordingly, the rotation of the tool has been specified using sliding mesh technique in the TMAZ [41-42], as it does not make any approximation on the profile of the moving tool [44].

Generally, as the distance from the tool increases, a gradient change in the temperature takes place. However, compared to the locations that are far away from the

tool; the temperature spatial gradient in the vicinity around the tool is severe [30]. Therefore, and purposefully (TMAZ) has been finely meshed to capture this level of gradient. As per the geometries of the tool and the workpiece, tetrahedral elements are easier to create with accepted level of quality rather than other types of elements [45]. Thus, these kinds of elements have been chosen for meshing the whole regions of the computation domain where the number of elements reached around 700,000 elements. It is worth mentioning that the mesh created is an initial mesh which will be used in the dwelling stage of the welding process where the tool has only rotational motion.

As previously explained, the tool has two types of motion in the welding stage of FSW where it rotates and translates along the joint line. It is also commonly known in CFD models of FSW that defining the translational tool motion in terms of inlet flow velocity which is still an approximation. Hence, in the current used model the translational motion of the tool has been specified using dynamic mesh technique, and considering the path followed by the tool as a solid region, rather than fluid. Accordingly, a continuous change of the mesh is taking place with the time while the tool is travelling [41-42].

Dynamic mesh

Dynamic mesh differs from the time-constant mesh in that the cells might disappear, merge or at least change their shape during the time dependent simulation. According to the translational movement of TMAZ which represents the tool motion, the cell boundaries will move with this prescribed motion. Consequently, the boundary elements adjacent to TMAZ will deform to keep the mesh consistency and the nodes corresponding to the deformed mesh will be updated. In the current study, User Defined Function (UDF) subroutine was prepared to apply both of travel and rotational motion. In order to avoid the mesh to be invalidated, smoothing, layering and remeshing methods are provided by Fluent to update the dynamic mesh. Layering cannot be used for the tetrahedral mesh while both smoothing and remeshing are recommended. In smoothing process, expanding and compression of the edges can take place due to the deformation of the mesh nodes at the dynamic boundaries according to the specified motion. After that, if the smoothing and local remeshing failed in creation of a better mesh, the entire zone will be remeshed as depicted in Figure (3).

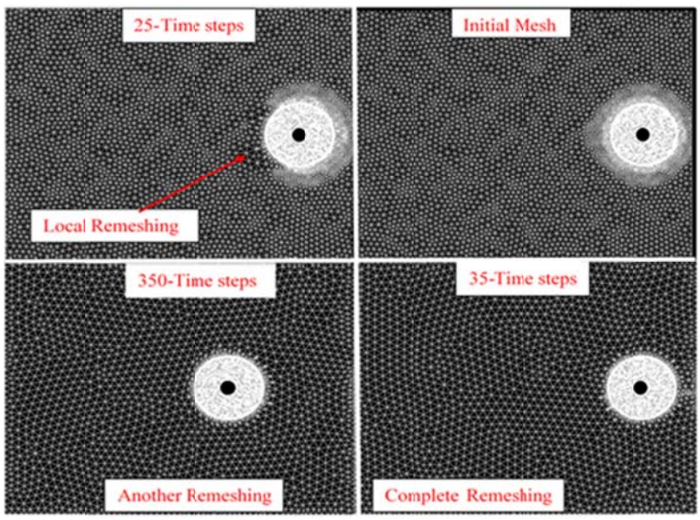

Figure 3: Initial and deforming mesh

Solver Execution

The material flow in FSW is governed by mass and momentum conservation equations, whereas to describe the heat transfer process, energy conservation equation is used. In these equations the mathematical statements of the conservation laws of physics are represented. Regarding the physical models, in the vicinity of the welding tool, and due to the resultant heat generation from the rotational speed of the tool, the liquid material behaves as non-Newtonian, viscoplastic, laminar and incompressible fluid flow [39,46]. Therefore, viscus laminar model that is available in Fluent was used in this study with reasonable accuracy. Besides that, as far as the effects of thermal changes during the process are concerned it is worth mentioning that in some real cases of FSW, melting temperature could be reached if the welding parameters have not been carefully controlled which in role causes a high heat input. That is why solidification/melting model was also proposed to be used among the other models that are available in the commercial CFD package. Fluent is equipped with solidification / melting model which can solve the phase change that is likely to happen whether at constant temperature or over temperature range [47]. A detailed information about theory and applications of solidification/melting mode are provided in different related titles and literatures [44,47,48].

Aluminium alloy (AA6061) was used in this study where its chemical composition, the temperature dependent thermophysical properties such as the thermal conductivity, specific heat and material constants heat has been considered [39]. Basically, the fluid medium in (TMAZ) was defined as liquid aluminium with a density of 2700 kg/m^3. Remarkably, the volume of fluid zone in the computation domain is small which is one of the current model's advantages as it minimises the inaccurate values of temperature distribution [30,37]. Moreover, as the constant viscosity would affect the results, different values of viscosity are considered according to the approximation of the viscosity of the plasticised metal proposed by Sheppard and Wright [24, 43] in which the ratio of the effective stress and the strain rate is used as

$$\eta = \frac{\sigma_E}{3\dot{\varepsilon}} \quad (1)$$

where η is the material viscosity, σ_E is the effective stress and $\dot{\varepsilon}$ is the strain rate. The Zener-Hollomon parameter [24, 37,43] is used to obtain the value of σ_E.

In terms of boundary conditions, the workpiece walls and the translating tool wall are the boundary types that have been specified. With a view to simulate the two real motions of the tool, it has been specified with rotational and travel speeds of 637rpm 1.59mm/s, respectively. Those speeds represent practical values which were taken from the literature [43] where User Defined Function (UDF) subroutine was prepared to apply both of travel and rotational speed of the tool. Thermally, to define the process of heat generation, a heat flux was applied to the tool surface after it had been calculated by the analytical heat generation equation given as [40]

$$Q = \frac{2}{3}\pi\mu\omega P(R_{Shoulder}^3 + 3\,R_{prob}^2\,H_{prob}) \quad (2)$$

Where, μ is the friction coefficient taken as 0.4 [49], ω is the rotational speed of the tool, P is the plunging pressure (applied load) which was kept at 12.7MPa. As the heat generation is given by the above equation, 85% of process efficiency was adopted [30] and then divided by the total surface area of the tool to give the heat flux. The convection heat transfer coefficient from the top and side surfaces of the workpiece is

25W/m^2 °C, and whereas the bottom surface is supported by a backing plate, the coefficient value is considered as 200W/m^2 °C [37, 50].

Mesh Independence Test

In order to conduct the independence test for the primary mesh, three different meshes were used as shown in Table (1). As the maximum temperature has been recorded at a point with a transverse distance of 8mm from the weld centre and a depth of 2mm from the top surface of the workpiece, the test results showed that the calculated value of maximum temperature approaches to the experimental value as long as the mesh is refined. Additionally, the difference is slightly less than 1% between the meshes with 350000 and 700000 elements while the difference was around 0.65% between the meshes with 700000 elements and 1.4 million elements. Accordingly, in terms of reducing the computation cost along with an acceptable accurate predicting; the mesh with 700000 elements has been nominated for further analysis.

Table 1: Mesh Independence Test Results

No. of mesh elements	Experimental Max. Temperature	Numerical Max. Temperature	Difference (%)
350000	835K (562 °C)	808.86K (535.86 °C)	
700000	835K (562 °C)	814.09K (541.09 °C)	0.97
1400000	835K (562 °C)	817.62K (544.62 °C)	0.65

Time Step Independence Test

In a view of the solution stability and accuracy, time step independence test has a significant role. As earlier mentioned, that both sliding and deforming mesh are employed in the current model; hence there is a need to determine the optimum time step for both techniques. It is noteworthy that dynamic mesh is predominantly much critical and dominant than sliding as it is sensitive to fail at any time step even it was advanced in the computation time. That is why; guarantee a successful dynamic mesh over the total computation time has the highest priority. Several considerations should be taken in account to avoid negative cell volume problem. Consequently, it is obvious that conducting the test is complicated whereas different procedures would be undertaken to harmonise the time step. To start with, Courant number concept is used and fulfilled to ensure that the solution will become stable. In essence, Courant number should be less than 1 [51], where the time step that was chosen for achieving the criteria is 0.1 second. Secondly, the volume mesh is updated within 0.1 second time step and using proper settings that are normally employed for triangular or tetrahedral mesh. After circumventing the problem that might happen within the dynamic mesh and by considering that 0.1second is the maximum reference step size that must not be exceeded, the concern is now about how to evade the effect of the change in the time step on the results particularly for the primary mesh. When talking about the primary mesh that means the period from the welding process in which the tool is only rotating and not translating. In other words, the moments in which the mesh is working without deforming and the sliding mesh is playing the key role. Hence, to investigate that effect and carrying out the time step independence test; three-time steps of 0.1sec, 0.066666sec, and 0.0333333sec were suggested under the above estimated maximum

reference step size. Table (2), displays the three-different values of proposed time steps along with the values of the maximum temperature that were recorded for those time steps at a point with a transverse distance of 8mm from the weld centre and a depth of 2mm from the top surface of the workpiece. In terms of the time step effect, it can be clearly seen that by increasing the time step from 0.033 to 0.1sec the difference percentage is just 0.71% which indicates that numerical results are insignificantly influenced. In view of the computation cost specifically when dealing with a thermal cycle duration of 100sec parallel with using of dynamic mesh, the time step of 0.1sec was nominated for future analysis.

Table 2: Time step independence results

Time step (sec)	Max. Temperature K(C°)	Difference (%)
0.033	818K(545C°)	
0.066	816.2K(543.2C°)	0.33%
0.1	814.09K(541.09C)	0.71%

Benchmark Tests

The numerical results benchmarking is required to validate the current proposed model. Therefore, the CFD predicted time-dependent temperature was recorded for 100 seconds of operation at 4 points located in the advancing side, two of them (point 1 and 2) having a transverse distance of 8mm and 16mm from the weld centre at a depth of 2mm from the top surface of the workpiece. The other two points (3 and 4) having the same transverse distances but at a depth of 8mm from the top surface of the workpiece.

The predicted temperatures at the four points verified against published experimental data for aluminium alloy (AA6061) by Nandan et al. [43]. Figures 4(*a*), 5(*a*), 6(*a*), and 7(*a*) illustrate the calculated temperature profiles from the current developed CFD model and the traditional CFD model (baseline) [24, 28-29, 31-32, 35, 38] at the four monitoring locations against the measured ones. Generally, the trend of the temperature at each point represents a thermal cycle of 100sec, in which the points are heated up until the peak temperature is achieved and then start to cool down.

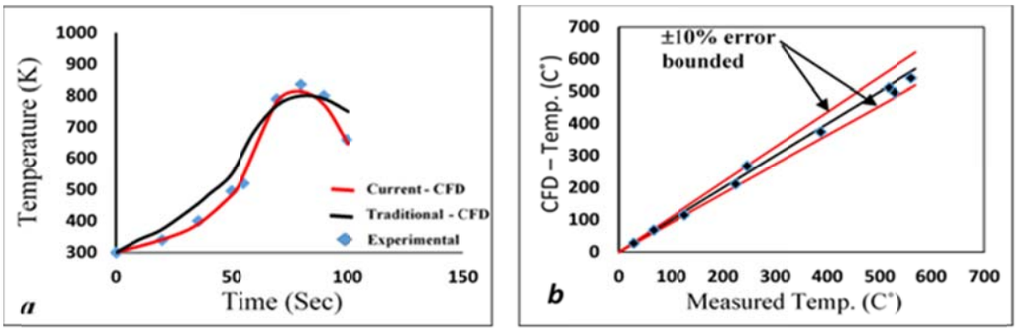

Figure 4: (*a*) The calculated and measured temperatures at point1 (*b*) The difference between calculated and measured temperatures at point1.

In the figures, it can be seen that the current CFD model has room of improvement where the accuracy has increased. Furthermore, the current CFD results and the experimental results are in better agreement where the averages of error percentages for points 1, 2, 3 and 4 are 4.23%, 5.89%, 5.02% and 4.35% respectively.

Besides, Figures 4(*b*), 5(*b*), 6(*b*), and 7(*b*) show the difference between the temperature values calculated from CFD and those obtained from the experimental results. Within error band ranged from 0 to maximum ±10%, it can be seen that most of the data lies in this range. Thus, it can be concluded that the current numerical model represents the physical model of FSW.

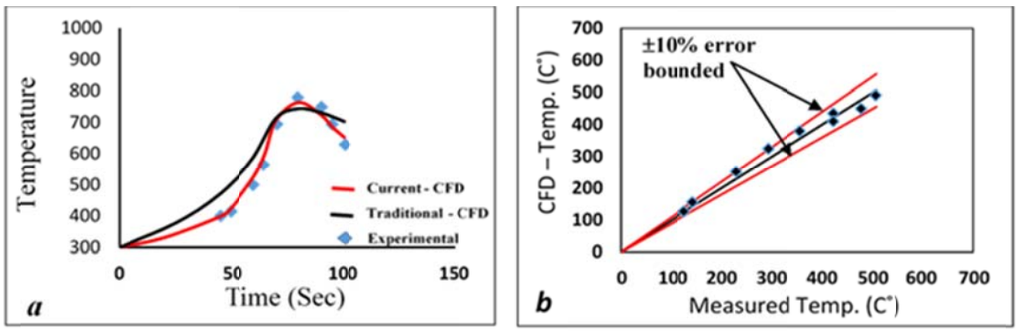

Figure 5: (*a*) The calculated and measured temperatures at point 2 (*b*) The difference between calculated and measured temperatures at point 2.

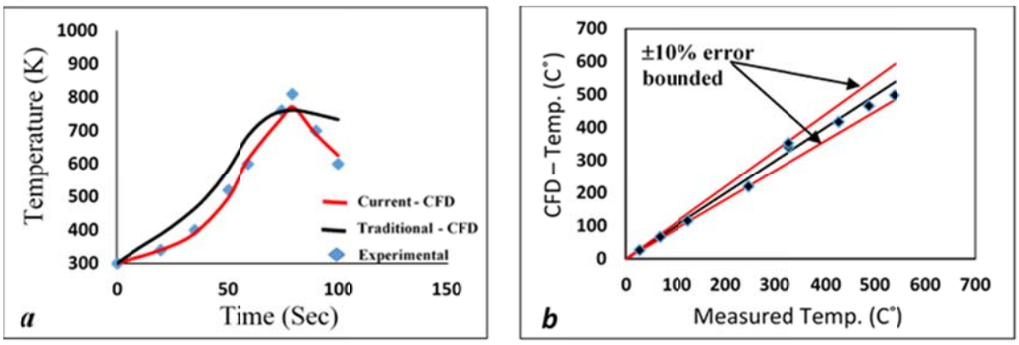

Figure 6: (*a*) The calculated and measured temperatures at point 3 (*b*) The difference between calculated and measured temperatures at point 3.

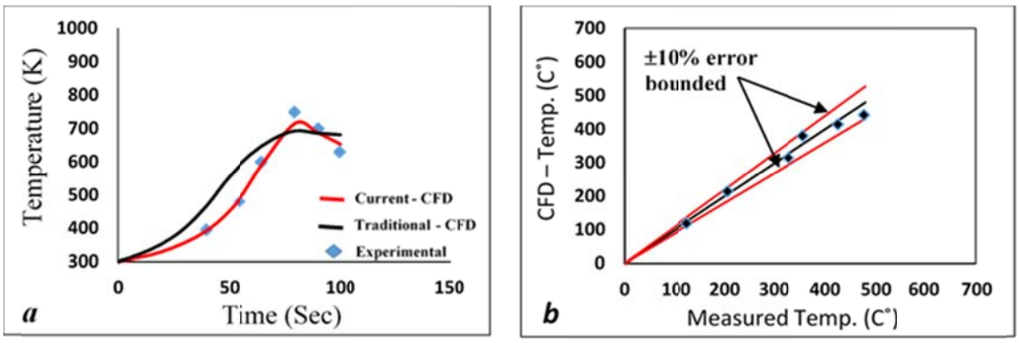

Figure 7: (*a*) The calculated and measured temperatures at point 4 (*b*) The difference between calculated and measured temperatures at point 4.

ANALYTICAL MODELLING OF HEAT GENERATION

Based on the objectives previously formulated, several FSW tools having different polygonal pin profiles have been investigated. In this section, a tool with Heptagonal pin profile has been chosen to demonstrate the detailed steps of developing the analytical models of the heat generated by these tools during the FSW process. The

analytical models of the considered cases have been established based on the analytical models developed by Schmidt et al [3] and Gadakh et al [40]. In Figure (8), the schematic of a tool with Heptagonal pin and the main regions of heat generation are shown, where Q_1 is the heat generated at the tool shoulder base, Q_2 is the heat generated at the sides of the tool pin and Q_3 represents the heat generated at the pin tip. Summation of these gives the overall heat amount Q_{total} produced due to the friction between the tool surfaces and the workpiece.

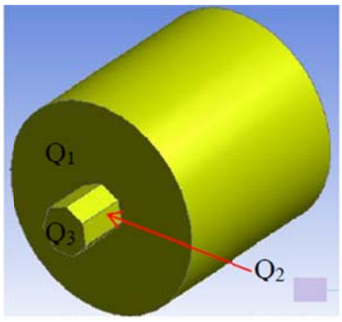

Figure 8: Tool with heptagonal pin

Uniform contact shear stress $\tau_{contact}$ is generally considered in FSW, while at the contact interface, sliding condition of the shearing is also regarded. Hence, the frictional shear stress $\tau_{friction}$ is estimated for this condition as $\tau_{contact} = \tau_{friction} = P.\mu$, where P is the applied force per unit area of the shoulder base. Heat generated only due to friction is considered which means that the heat amount from deformation is neglected. The general equation for heat generation is [40]

$$dQ = \omega.dM = \omega.r.dF = \omega.r.\tau_{contact}.dA \quad (3)$$

Where ω is the angular velocity, dM is the infinitesimal segment torque, r is the distance from the considered area to the centre of rotation, dF is the infinitesimal segment force that produces the torque, and dA is the infinitesimal segment area exposed to a uniform contact shear stress $\tau_{contact}$.

Heat Generation from Shoulder Base

To calculate the net frictional heat generation from shoulder base, the heat generated at the pin tip should be subtracted from the heat generated at the shoulder base. Figure (9) shows the effective shoulder base area at which the heat is generated. Thus, the considered area segment dA = r. $d\theta.dr$ generates heat

$$dQ = \omega.r.\tau_{contact}.r.d\theta.dr \quad (4)$$

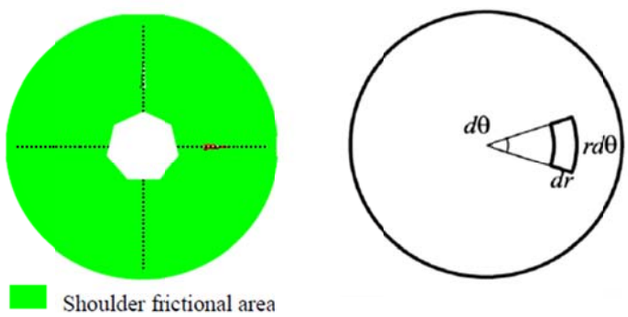

Figure 9: Shoulder effective area and the infinitesimal segment area for the tool with heptagonal pin profile

By integrating equation (4) over the area from 0 to Rs, the net heat generation at the shoulder base Q_1 can be expressed as:

$$Q_1 = \int_0^{2\pi} \int_0^{Rs} \omega . r^2 . \tau_{contact} . d\theta . dr - Q_3$$

where Rs is the shoulder radius. Thus:

$$Q_1 = \frac{2}{3} \pi . \omega . \tau_{contact} . R_s^3 - Q_3 \quad (5)$$

Heat Generation from Pin Side Surfaces

To calculate the heat generation from the pin side surfaces, the main dimensions of the pin side need to be defined first. For a heptagonal pin, it can be seen in Figure (10*a*,*b*) that the pin is described by the following dimensions:

a: is the side length.
S: is the apothem that indicates the distance from the centre to the midpoint of a side.
Rp: is the radius of the polygon's circumcircle.
H: is the pin height.

Also, the infinitesimal segment area on each side of Heptagon is shown in Figure (10c) where $dA = dx.dz$

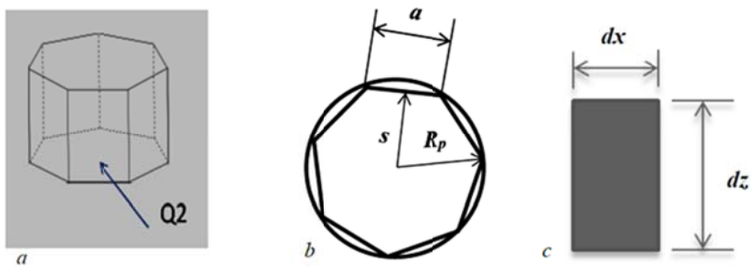

Figure 10: Main trigonometric dimensions of Heptagon and the infinitesimal segment area of each side.

Therefore, over the pin side surface area, the heat generation equation can be written according to the following;

$$dQ = \omega . s . \tau_{contact} . r . dx . dz \quad (6)$$

By integrating equation (6) over the side pin surface area from 0 to H, it gives the heat generation at one segment of pin side surface. In order to estimate the overall heat generation from the pin side, the equation should be multiplied by 7 for Heptagonal pin.

$$dQ = Q_2 = 7 \int_0^a \int_0^H \omega . \tau_{contact} . s . dx . dz$$

$$Q_2 = 7 \, (\omega . \tau_{contact} . s . a . H) \quad (7)$$

As in a regular polygon, the distance from the centre to any vertex indicates the radius of the polygon Rp, the relationship between this radius and the side length is

$$Rp = \frac{a}{2sin\left(\frac{180}{n}\right)} \quad (8)$$

Where, n is the number of pin sides.
The relationship between the radius and the apothem is [52]

$$Rp = \frac{s}{cos\left(\frac{180}{n}\right)} \quad (9)$$

By equating the equations 8 and 9, the apothem can be expressed as a function of the side length:

$$s = \left(\frac{a}{2} cot \frac{180}{n}\right) \quad (10)$$

When n=7, s is equal to 1.0382 a.

Substituting s in equation 7, the equation of heat generation at the pin side surfaces can be expressed as:

$$Q_2 = 7.2678\ (\omega . \tau_{contact} . a^2 . H) \quad (11)$$

Heat Generation from the Pin Tip

A flat pin tip surface has been considered in this study, which has been also divided into fourteen sections as shown in Figure (11). Using polar coordinates, the heat generation equation for each section is expressed as:

$$dQ = \omega . r . \tau_{contact} . r . d\theta . dr \quad (4)$$

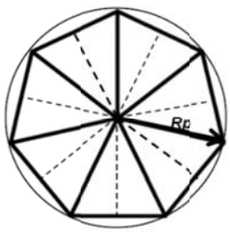

Figure 11: Schematic of the heptagonal pin tip

By integrating equation (4) over the pin tip surface area from 0 to Rp, and using the multiplying factor 14 which denotes the fourteen sections that form the heptagonal tip surface, the heat generation from the pin tip Q3 can be computed as:

$$Q_3 = 14 \int_0^{\theta=\frac{\pi}{7}} \int_0^{Rp} \omega . r^2 . \tau_{contact} . d\theta .\ dr$$

In equation 8, Rp is equal to 1.1523$\boldsymbol{a}$ when n=7. Therefore,

$$Q_3 = 14 \int_0^{\theta=\frac{\pi}{7}} \int_0^{Rp=1.1523\boldsymbol{a}} \omega . r^2 . \tau_{contact} . d\theta .\ dr$$

$$Q_3 = \left[\frac{2 \times 1.53 \pi . \omega . \tau_{contact} . a^3}{3}\right] \quad (12)$$

Total Heat Generation from the Tool

Using equations (5), (11) and (12) the total heat generation from the tool with heptagonal pin can be computed as:

$$Q_{total} = \frac{2}{3} \pi . \omega . \tau_{contact} . R_s^3 + 7.2678\ (\omega . \tau_{contact} . a^2 . H)$$

By rearranging

$$Q_{total} = \frac{2}{3} \pi . \omega . \tau_{contact}\ (R_s^3 + 3.47189\ a^2 . H) \quad (13)$$

Or

$$Q_{total} = \frac{2}{3} \pi . \omega . \tau_{contact} \left(R_s^3 + 3.47189\ \left(\frac{Rp}{1.1523}\right)^2 . H\right)$$

$$Q_{total} = \frac{2}{3} \pi . \omega . \tau_{contact}\ (R_s^3 + 2.61477\ Rp^2 . H) \quad (14)$$

Similarly, for the other tools with polygonal pin profiles that have a higher number of side faces, the heat generation expressions have been developed using the same analytical approach. Based on the number of pin faces, the heat generation expressions are listed in Table (3). By comparing the developed expressions in the table

with each other, it can be seen that all the terms in the equations are the same except those related to the pin radius. Accordingly, a general equation can be expressed as:

$$Q_{total} = \frac{2}{3}\pi.\omega.\tau_{contact}\,(R_s^3 + C_n.\ Rp^2.H) \quad (15)$$

Where C_n has different values according to the number of polygon faces.

Table 3: Heat generation formulas of tools with different polygonal pins

Pin Profile	No. of Faces	Equation
Heptagonal	7	$Qtotal = \frac{2}{3}\pi.\omega.\tau_{contact}\,(R_s^3 + 2.61477\ Rp^2.H)$
Octagonal	8	$Qtotal = \frac{2}{3}\pi.\omega.\tau_{contact}\,(R_s^3 + 2.7018\ Rp^2.H)$
Nonagonal	9	$Qtotal = \frac{2}{3}\pi.\omega.\tau_{contact}\,(R_s^3 + 2.7632\ Rp^2.H)$
Decagon	10	$Qtotal = \frac{2}{3}\pi.\omega.\tau_{contact}\,(R_s^3 + 2.80756\ Rp^2.H)$
Undecagon	11	$Qtotal = \frac{2}{3}\pi.\omega.\tau_{contact}\,(R_s^3 + 2.8402\ Rp^2.H)$
Dodecagon	12	$Qtotal = \frac{2}{3}\pi.\omega.\tau_{contact}\,(R_s^3 + 2.8658\ Rp^2.H)$
13-gon	13	$Qtotal = \frac{2}{3}\pi.\omega.\tau_{contact}\,(R_s^3 + 2.8856\ Rp^2.H)$
14-gon	14	$Qtotal = \frac{2}{3}\pi.\omega.\tau_{contact}\,(R_s^3 + 2.90122\ Rp^2.H)$
15-gon	15	$\mathrm{Qtotal} = \frac{2}{3}\pi.\omega.\tau_{\mathrm{contact}}\,(\mathrm{R_s^3} + 2.9141\ \mathrm{Rp^2.H})$
25-gon	25	$Qtotal = \frac{2}{3}\pi.\omega.\tau_{contact}\,(R_s^3 + 2.9684\ Rp^2.H)$
30-gon	30	$Qtotal = \frac{2}{3}\pi.\omega.\tau_{contact}\,(R_s^3 + 2.979\ Rp^2.H)$
40-gon	40	$Qtotal = \frac{2}{3}\pi.\omega.\tau_{contact}\,(R_s^3 + 2.988\ Rp^2.H)$

All above derived heat generation equations have been used for the same aluminium FSW welding process and conditions in section of CFD modelling. After calculating the heat amount from the analytical equations for all proposed cases, they were plotted in Figure (12) and compared with the calculated heat generated for the tool with cylindrical pin profile. It can be seen that the total heat produced by the tool increases as the numbers of polygon faces increase. Total heat generated from a tool having 7 side faces has been calculated to be 11878W, which increases to reach 11987W as the number of faces increases to 25. As the number of faces further increase,

the increase in the total heat generation from the tool is very small. The reason for this is that the number of faces has increased so much where the pin shape approaches the cylindrical shape, which depicts maximum heat generation. Approaching 12010W as the number of faces increase, 12010W being the heat amount of the cylindrical pin. At this point, the frictional forces are maximum due to more exposed area of the pin.

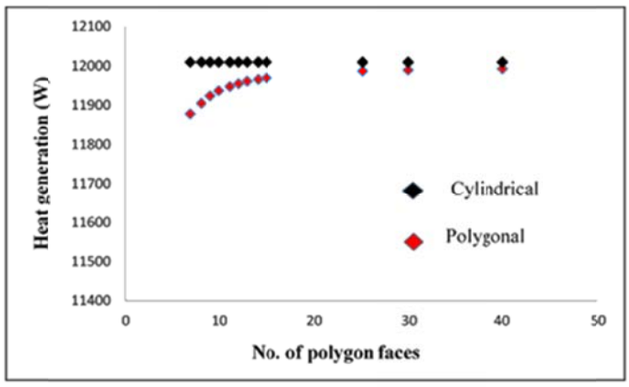

Figure 12: Heat generation variations w.r.t the number of polygon faces.

SCOPE OF NUMERICAL INVESTIGATIONS

The current CFD model with the aid of the analytical heat generation correlations have been used to estimate the effects of different geometrical and operational parameters on the thermal field of FSW process. In order to examine how number of pin faces might affect the maximum temperature, Heptagonal, Octagonal, and Nonagonal pin profiles have been used along with the welding parameters and conditions described in the section of CFD modelling. The maximum temperature has been locally monitored where it was recorded for a thermal cycle of 100 seconds at the four points that were defined in the section of CFD modelling. As plotted in Figure (13), the maximum temperature has mostly scored the same value for each single point against different number of faces.

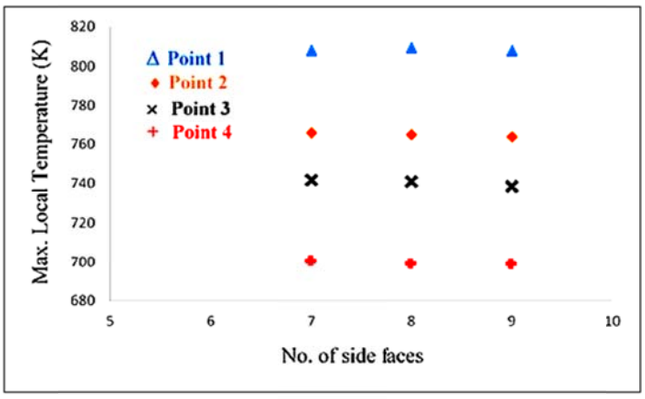

Figure 13: Local maximum temperature at four different points.

For example, the maximum local temperature at point 1 was recorded to be 807.9K, 808.1K and 808.27K for the cases of Heptagonal, Octagonal, and Nonagonal pin profiles, respectively. Referring to the heat generation amounts in Figure (12) it seems that the increase in the heat amount along with the increase in the number of

faces is not that much high to cause an increase in the local temperature, particularly when considering the high thermal conductivity of aluminium as well as the plate thickness which enhances the heat transfer process. From another point of view, the distances between the four locations cause the difference in the temperature values where the highest temperature is expected to be close to the shoulder surface. As the temperature trend was the same for the three proposed tools and to reduce the number of numerical experiments, octagonal pin was nominated for further investigations.

As this study aims at understanding the effects of a wide range of geometrical and operational parameters on the thermal characterisations of FSW, several process variables have been taken into consideration. The range of the chosen variables has been specified based on the practical values of these parameters and the model capability. As presented in Table (4), a set of numerical experiments have been proposed to investigate the effects of the selected parameters which are shoulder size, pin size, pin height, material thickness, tool rotational speed and axial load. In this set of numerical experiments, the effect of each variable has been addressed by four different values as shown in the table. To visualise how the change in the considered process variables may influence the thermal field, the temperature distribution throughout the workpiece was monitored. Moreover, different time instances from the welding cycle (100 sec) were selected to show the time dependent change that would occur to the temperature profile during the welding process. This information has then been used to develop novel statistical prediction model for the peak temperature.

Table 4: Process parameters and their ranges

No.	Shoulder Radius(mm)	Pin Radius(mm)	Pin Height(mm)	Material Thickness (mm)	Rotational Speed(rpm)	Axial load (MPa)
EX.1	13	6	12	12.7	637	12.7
EX.2	17	6	12	12.7	637	12.7
EX.3	21	6	12	12.7	637	12.7
EX.4	25	6	12	12.7	637	12.7
EX.5	25	3	12	12.7	637	12.7
EX.6	25	9	12	12.7	637	12.7
EX.7	25	12	12	12.7	637	12.7
EX.8	25	6	11	12.7	637	12.7
EX.9	25	6	10	12.7	637	12.7
EX.10	25	6	9	12.7	637	12.7
EX.11	25	6	12	14.7	637	12.7
EX.12	25	6	12	16.7	637	12.7
EX.13	24	6	12	18.7	637	12.7
EX.14	24	6	12	12.7	237	12.7
EX.15	24	6	12	12.7	437	12.7
EX.16	24	6	12	12.7	837	12.7
EX.17	24	6	12	12.7	637	9.7
EX.18	24	6	12	12.7	637	11.2
EX.19	24	6	12	12.7	637	14.2

RESULTS AND DISCUSSION

Effects of Shoulder Diameter

Figure (14), illustrates the temperature contours on a vertical plane at the weld centre line when using shoulder diameters of 26mm and 50mm whereas dwelling and welding stages are represented. Overall, when tracking the temperature distribution along the pin length, it's clear that the lower temperature zone is at the pin bottom end (tip) and tends to increase towards the shoulder base. Two reasons are likely to be behind this trend; the rate of heat generation at the pin tip is lower than that around the pin side surface as the frictional area is relatively smaller. Secondly, the existence of the highest heat generation zone near to the upper end of the pin where the shoulder-workpiece interface. From the figure, it can also be seen in the temperature scales that the maximum temperature in case of 50mm shoulder diameter is much higher than that for 26mm. This means that the increase in the shoulder size leads to an increase in the temperature which is referred to the increase in the frictional area. In terms of the process time, the temperature distribution at early stage from the welding process indicates that the material has witnessed very high heating rates. At times 1sec, 3sec and 5sec which are part of dwelling time, the maximum temperature has been recorded to be 578.6K, 750.9K and 815.3K respectively for a shoulder radius of 25mm. After 40 seconds, at a moment in which the tool has already changed its position; the temperature has increased to 836.1K.

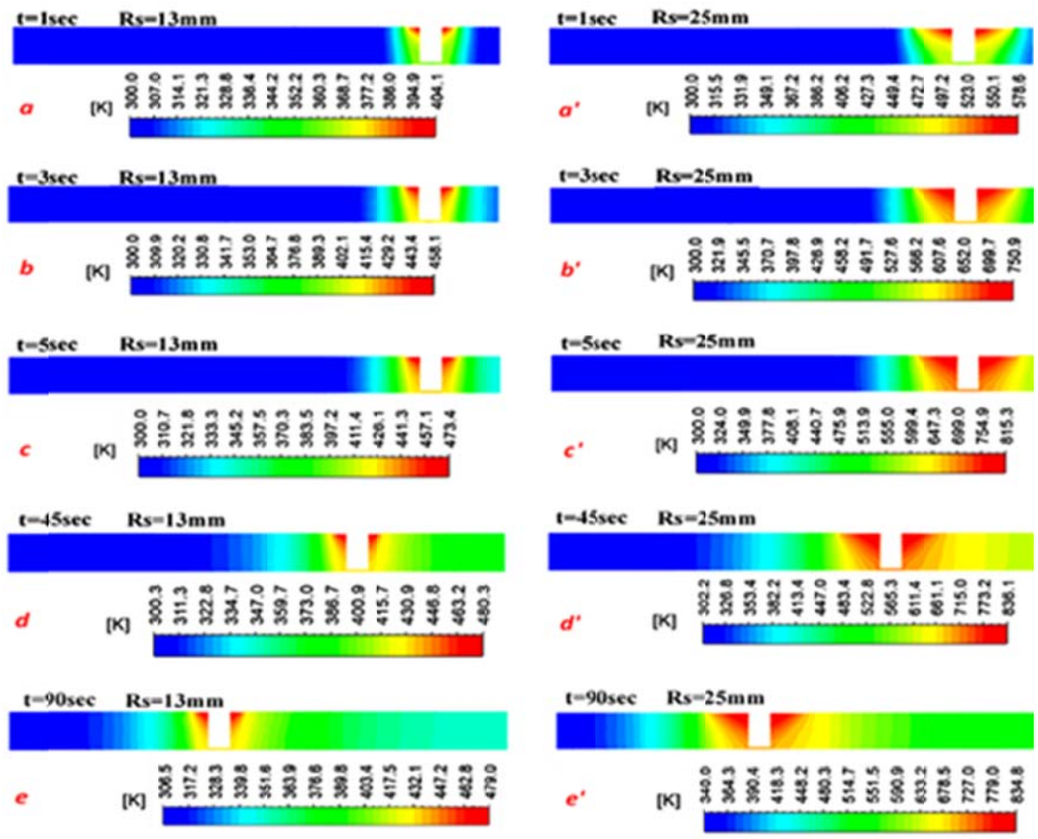

Figure 14: Transient temperature distribution for shoulder diameters 26mm and 50mm

To explain the variation in the temperature distribution due to the change in the shoulder size, instantaneous snapshots were taken at the plane where maximum temperature is expected to be recorded. This plane includes the contact region between the shoulder and the workpiece where the peak temperature is likely to be achieved [53]. As the greatest component of heating is due to the friction between the shoulder and the workpiece, it can be generally seen in Figure (15*a*,*b*,*c*,*d*) that the hottest area is in the vicinity of the tool. Although, the high temperature contours around the tool are almost symmetrically distributed, the temperature gradient is steeper in front of the tool than behined. That can be attributed to the decrease in material diffusivity due to the heat accumulation at the rear of tool and for this reason the heat dissipation becomes slower. Conversely, at the leading zone where some parts of the workpiece are still at room temperature, the temperature profile demonstrates that the heat is rapidly dissipated. At the temperature scale in *d* when the shoulder radius is 25mm, the minimum temperature is 320K which is higher than the room temperature. That means the workpiece is completely affected by the highest supplied heat by this size of shoulder compared to the other sizes. In view of this, it can be also observed in the figure that the growth in the different regions of contours from *a* to *d* is dramatic.

In Figure (16) it can be also seen that the peak temperature increases when the shoulder diameter increase. For instance, the peak temperature has scored 481K, 597K, 720K and 848K for diameters of 26mm, 34mm, 42mm and 50mm, respectively.

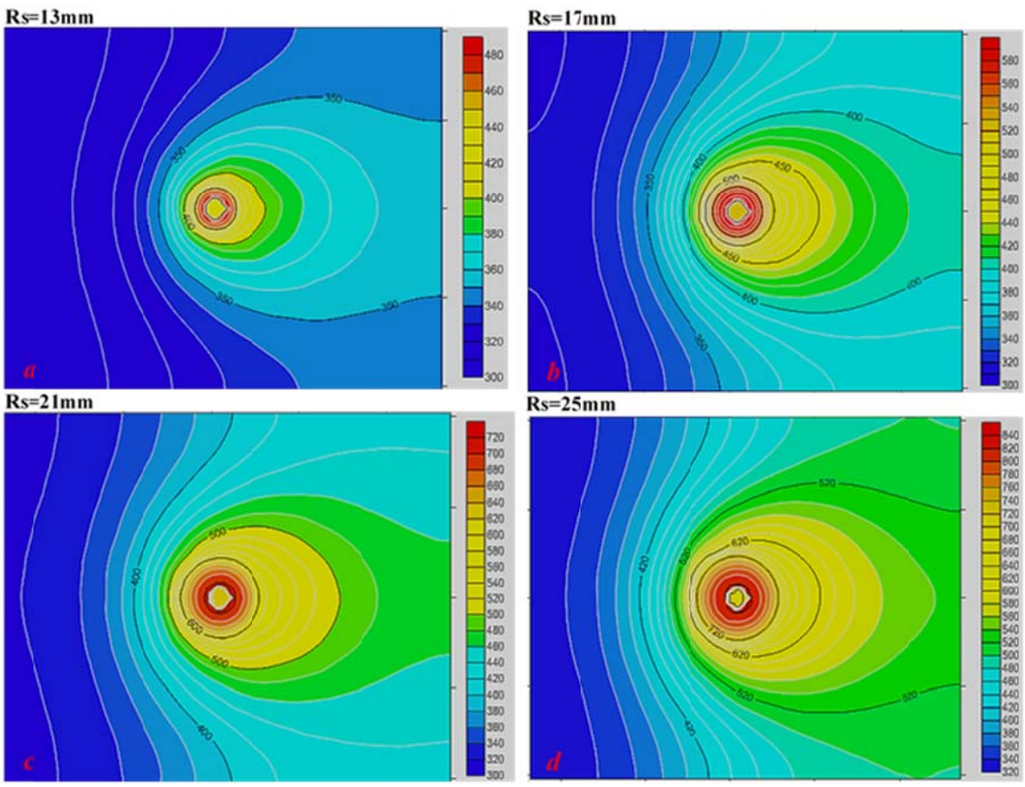

Figure 15: Static temperature contours for different shoulder diameters *a*=26mm, *b*=34mm, *c*=42mm, *d*=50mm.

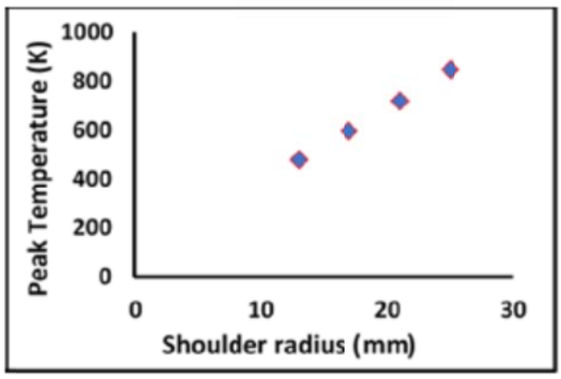

Figure 16: Peak temperature for different shoulder radii

Effects of Pin Diameter

Figure (17) depicts a comparison between the time dependent temperature distribution when Rp=3mm and Rp=6mm. It can be noticed for Rp=3mm that the highest and minimum temperatures that were attained are higher than those recorded for Rp=6mm. Similarly, the heating rate was higher where it has achieved 297.4K/sec at t=1sec for Rp=3mm while it was 278.6K/sec for Rp=6mm at the same time. This would be attributed to the area of shoulder as it becomes smaller when the pin radius grows up where the reduction in the shoulder's area was by 0.01cm^2.

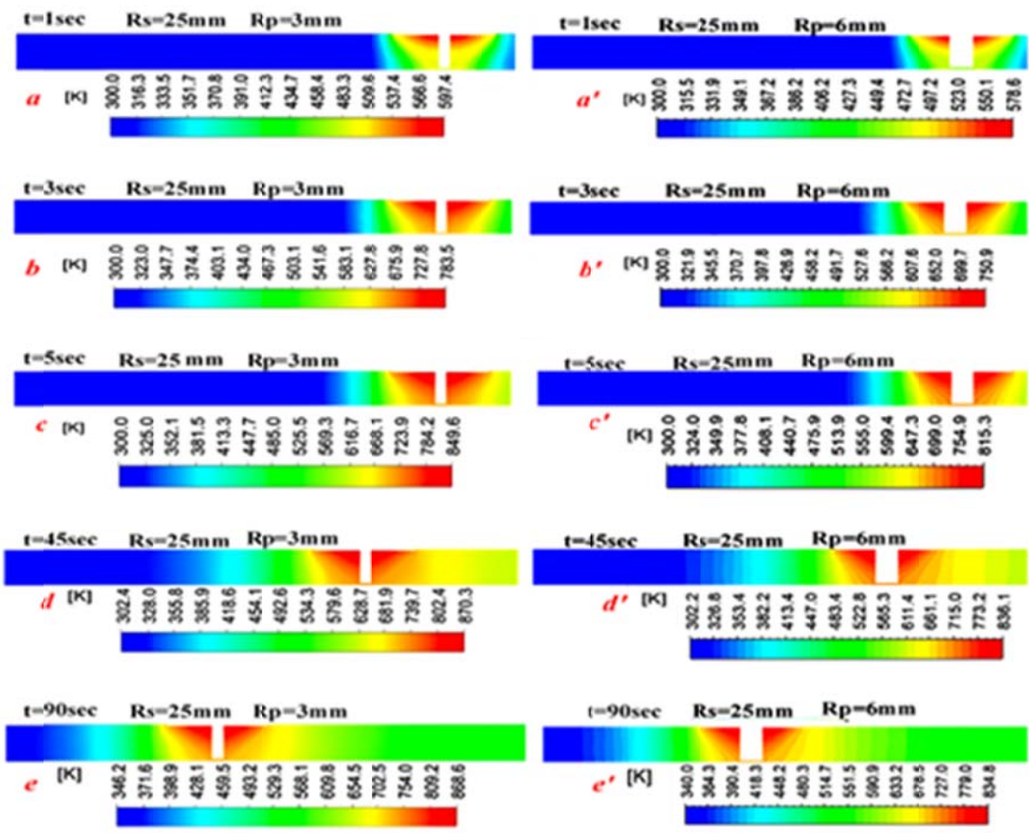

Figure 17: Transient temperature distribution for pin diameters 6mm and 12mm

Figure (18*a,b,c,d*) depicts the variation in the temperature distribution for different pin dimensions. Although the increase in the pin size leads to dropping the temperature, it can be observed that the change in the temperature profile is not as significant as when the shoulder size was altered. When the pin radius is 3mm, it is noticeably seen that the material solidus temperature (855K) is exceeded which means that the material parts that have witnessed this temperature become liquid.

As the transient temperature distribution can be monitored over the welding process. The current model has the advantage of estimating the liquid fraction during the process if the temperature is higher than the material solidus temperature. The amount of liquid with respect to the same cell volume in the calculation domain is named as the liquid fraction (β). Here, it is worth mentioning another significant feature in this model which is the mushy zone. In the mushy zone, the value of β is distinguished between 0 and 1. In fact, β at certain position and time is equal to zero if the material temperature was lower than the solidus temperature of the material used [44, 47]. For Rp = 3mm and 6mm, Figure (19) shows the liquid fraction contours within the materials being welded together at the same time step in which the temperature distributions were previously presented in Figure (18*a,b*). Although the temperature around the tool has insignificantly exceeded the solidus temperature when Rp =3mm, the model was able to predict the mushy zone. It can be clearly seen in the magnified section of mushy zone in which the value of liquid fraction is gradually changing from the minimum of 0% to maximum of 3.3%. These values indicate that a very small amount from the welded material has converted to liquid. On the other hand, the model never predicted any mushy zone when Rp =6mm which means that the temperature of the whole workpiece is still under the solidus temperature.

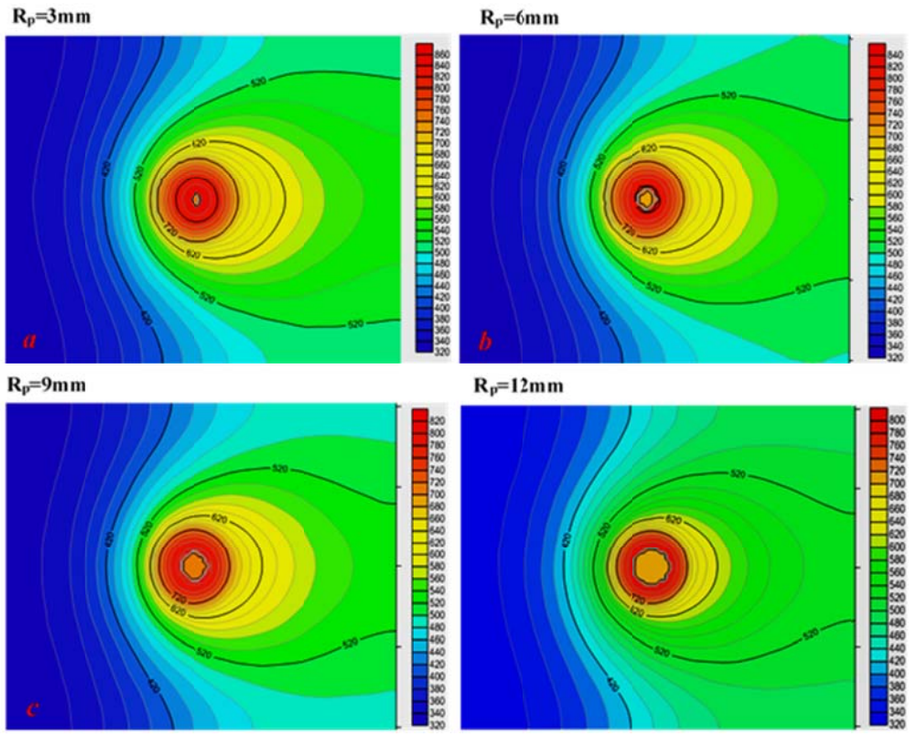

Figure 18: Static temperature contours for different pin diameters *a*=6mm, *b*=12mm, *c*=18mm, *d*=24mm.

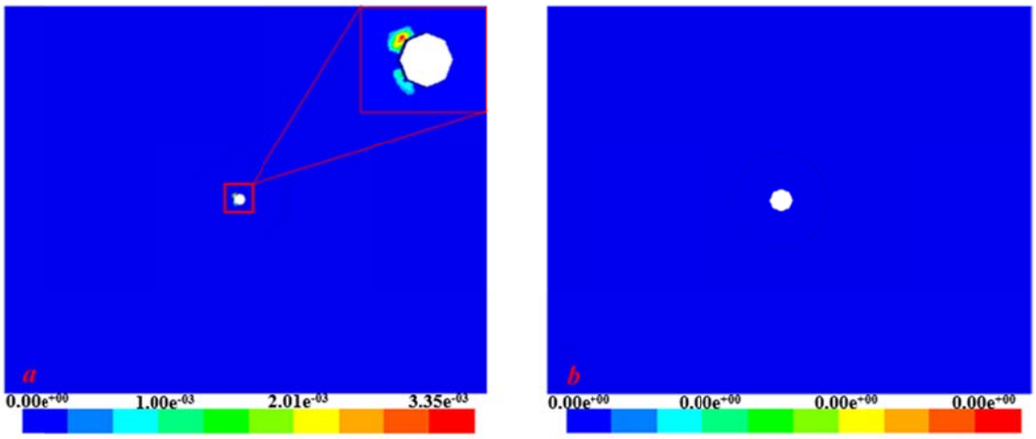

Figure 19: Liquid fraction contours for different pin diameters (*a*) 3mm, (*b*) 6mm

It is depicted in Figure (20) that the peak temperatures decrease along with the increase in the pin radius (Rp). As previously stated, this trend can be justified by the reduction in the frictional area for the shoulder as the pin diameter increases. However, when Rp is equal to 12mm it is seen that the value of peak temperature has increased to exceed that recorded when Rp is 9mm. This can be understood in terms of heat generation in the welding process of thin plates; the shoulder surface is dominant in generating of heat by friction while in thicker plates, the pin role becomes more efficient [53].

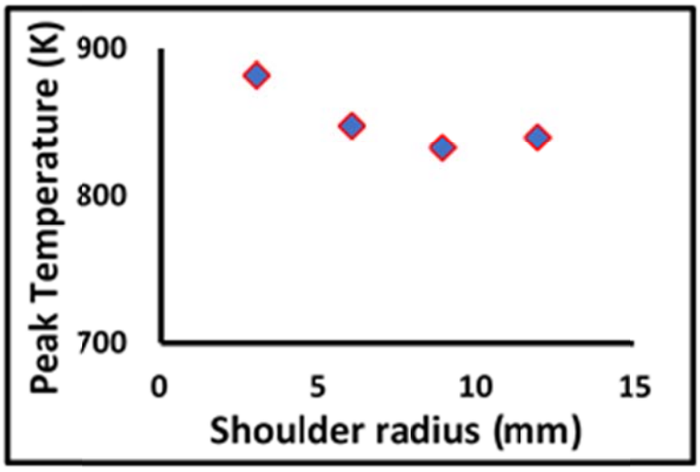

Figure 20: Peak temperature for different pin radii

Effects of Pin Height

Figure (21) depicts the evolution in the temperature distribution across the process duration related to the variant pin height and to do so, the welding processes with 9 mm and 12 mm pin heights were selected. From the figure, it can be seen that the transient evolution in the temperature distribution is not highly impacted when the pin height changes from 9 mm to 12 mm. This can be recognised when comparing the temperature scale for both cases as the temperature increase does not exceed 10K.

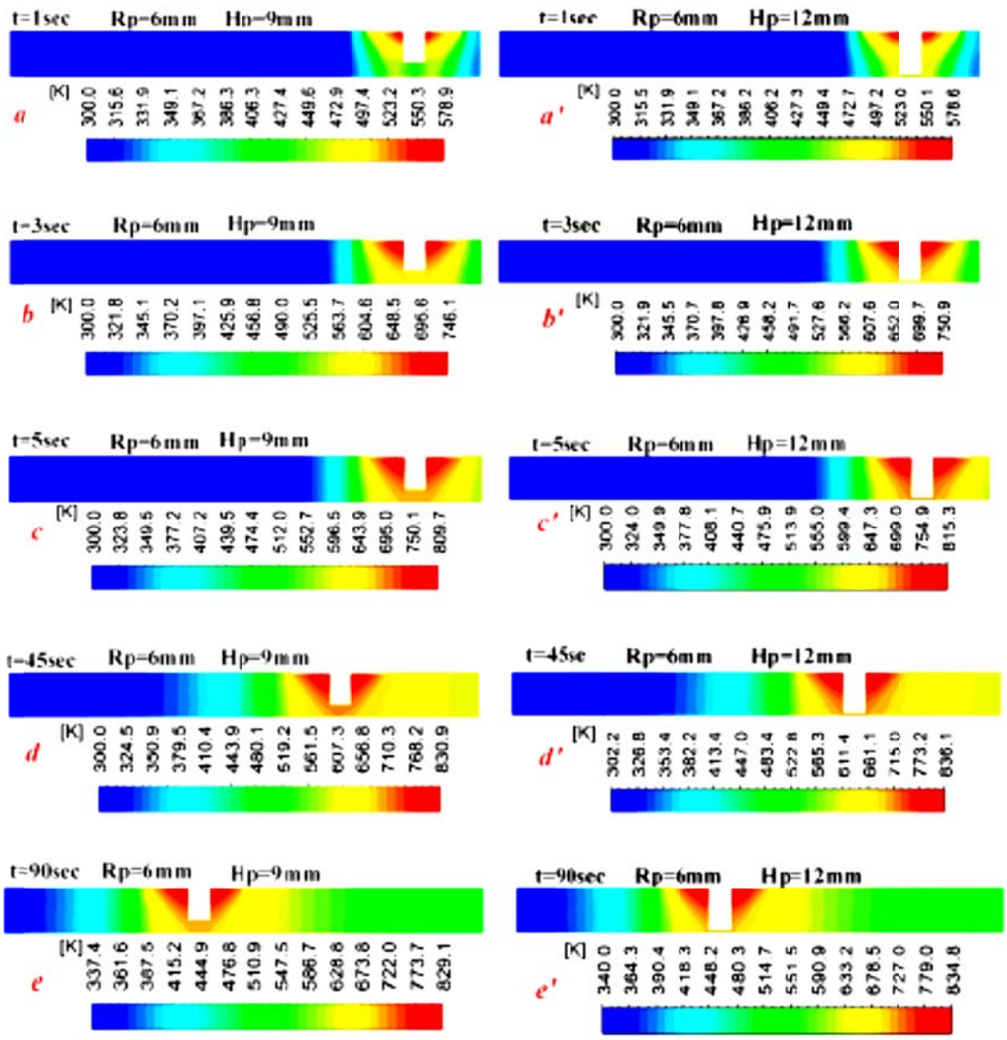

Figure 21: Transient temperature distribution for pin heights 9mm and 12mm

Figure (22*a,b,c,d*) displays the local variations in the static temperature due to the change in the pin height. The contours for different cases were taken at the same plane in the study of shoulder and pin dimension effects. In general, the temperature is normally distributed around the tool and insignificant variation can be observed on the contours according to the change in the pin height. That can be clearly seen when comparing position and form of the lines of 420K, 520K, 620K and 720K in *a*,*b*,*c* and *d*.

The values of peak temperature that were registered for different pin heights are depicted in Figure (23). The results illustrate that the peak temperature increases when the pin height becomes more which can be mainly ascribed to the increase in the frictional heat as the contact area between the pin side and the workpiece increases. To clarify, the peak temperature was 848K when Hp =12mm while 841K has been recorded for Hp =9mm. However, the impact of the increase in the pin height on the increasing of the temperature is less compared to the other geometrical parameters.

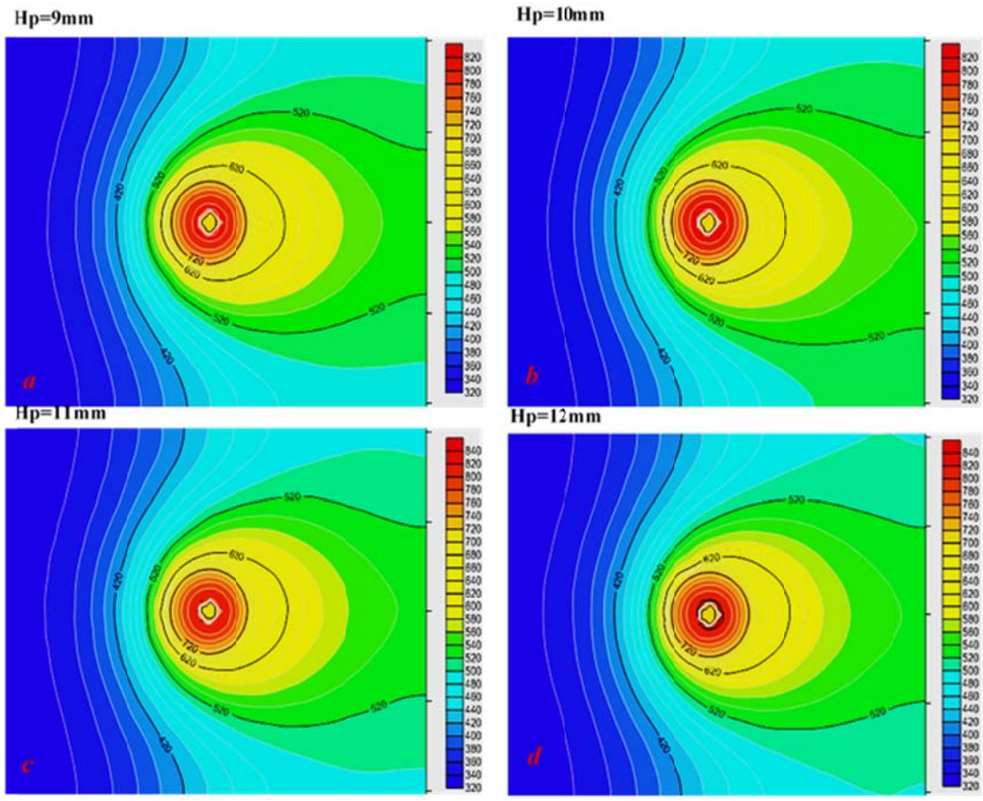

Figure 22: Static temperature contours for different pin heights *a*=9mm, *b*=10mm, *c*=11mm, *d*=12mm.

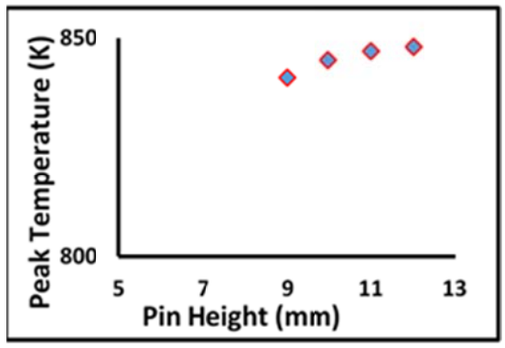

Figure 23: Peak temperature for different pin heights

Effects of the Workpiece Thickness

Figure (24) depicts how the change in the material thickness affects the temperature distribution in the vicinity of the welding tool as different time steps along the welding cycle were chosen when welding plates with thickness of 18.7 mm and 12.7 mm. The presented contours indicated that the hottest zone around the tool shrinks as the thickness increases and for the two cases under consideration, the difference in the maximum temperature was 28K in the first second of welding time while it has reached around 58K at t = 45 sec and after. That can be explained on account of the fact that before achieving the quasi –stationary thermal state, the heat conduction develops according to the temperature difference for each lonely case.

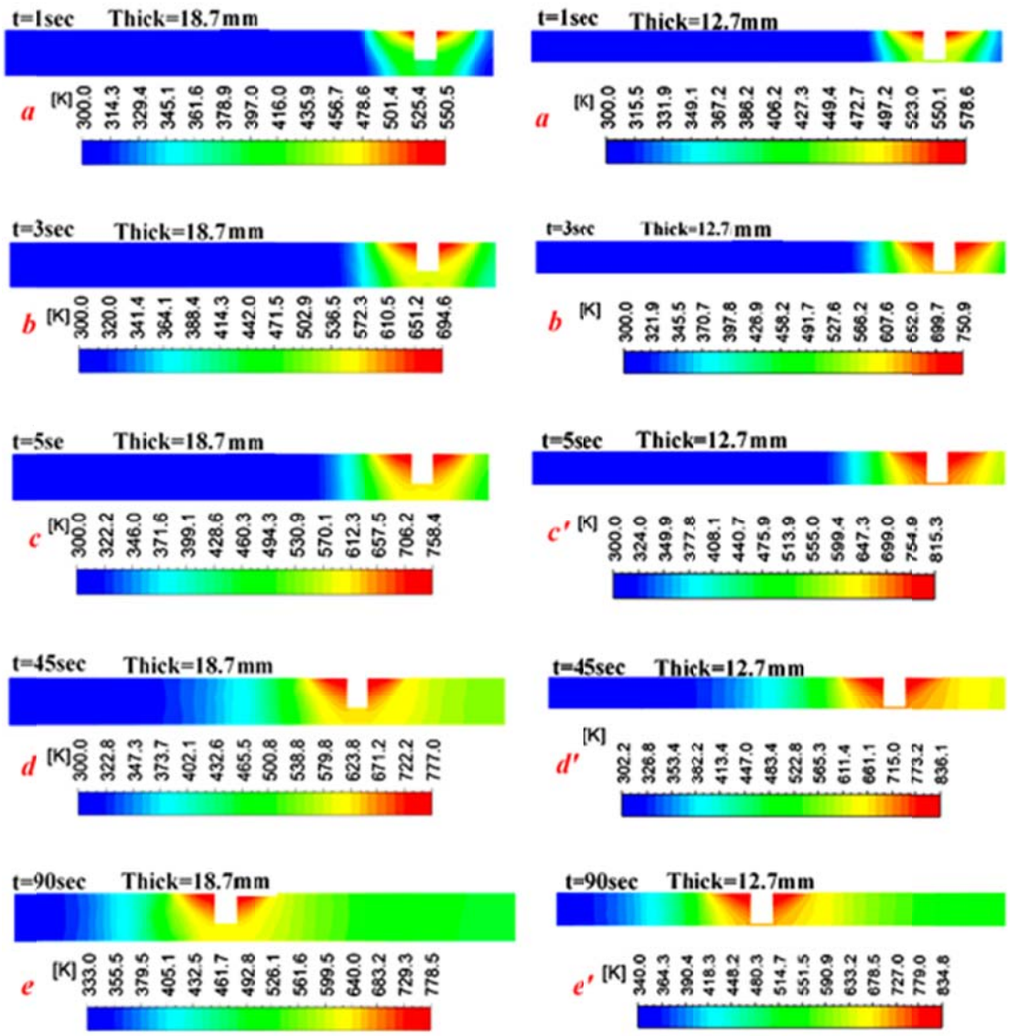

Figure 24: Transient temperature distribution for workpiece thicknesses 18.7mm and 12.7mm

Figure (25*a,b,c,d*), depicts the variation in the spatial temperature distribution within the weldment at the same moment for different workpiece thicknesses. Noticeably, the increase in the plate thickness causes a progressive decrease in the temperature values. Although, the heat input due to the frictional activities are almost the same the temperature gradients are clear as can be seen at the leading, trailing, advancing, and retreating sides. Compared to *a*, the line of 520K in *d* has a position closer to the pin and the maximum temperature in the scale is gradually dropping. This happens due to the enhancement of heat dissipation in the thickness direction. In other words, FSW is a heat transfer problem with a moving heat source which is just like the conventional welding processes. The geometry of the weld could affect the thermal features such as heating rate and cooling rate for a given welding parameters (heat input). As presented in Figure (26) the increase in the plate thickness leads to an increase in the rate of heat dissipation from the weld zone to the base metal which would give a reason for the decrease in the peak temperature [54].

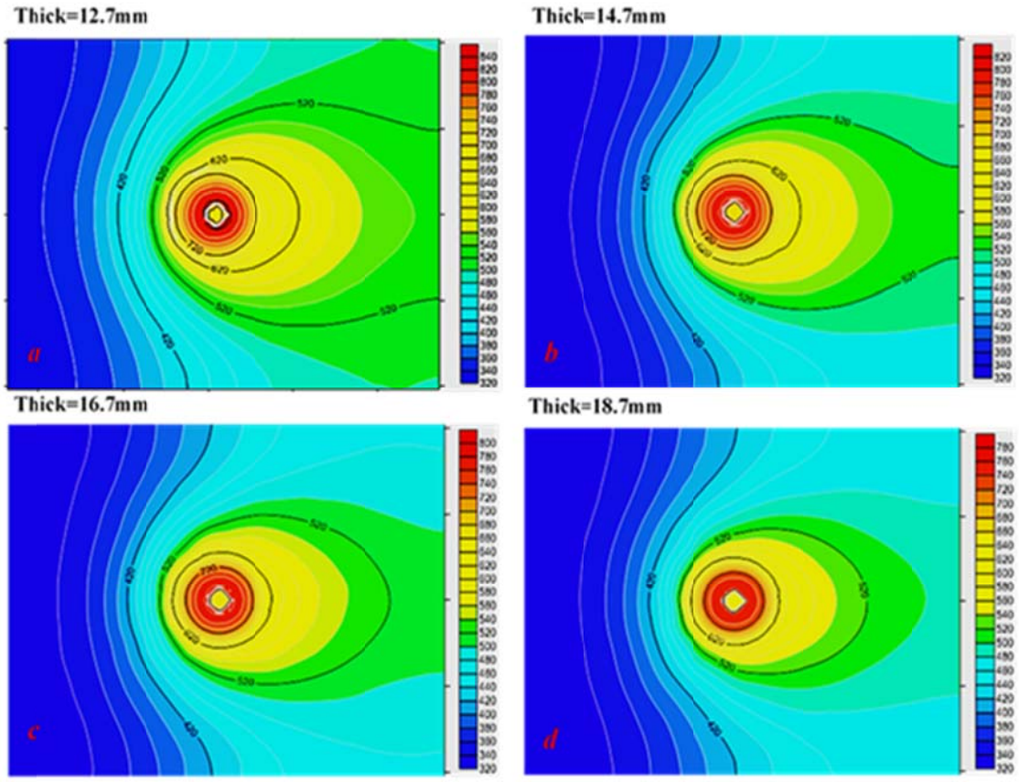

Figure 25: Static temperature contours for different workpiece thicknesses *a*=12.7mm, *b*=14.7mm, *c*=16.7mm, *d*=18.7mm.

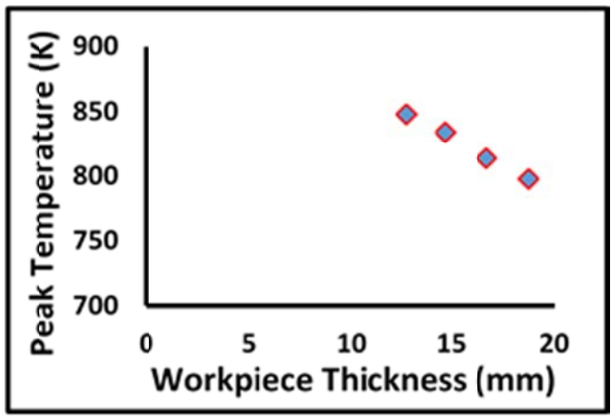

Figure 26: Peak temperature for different workpiece thicknesses

Effects of the Rotational Speed

Figure (27) depicts how the temperature distribution changes according to the variation in the welding rotational speed. That can be obvious in *a* and *b* when tracking the line of 400K while the line of 520K in *c* and *d* gives a clear indication as well. It can be seen from the figure that the hot areas grow up as the rotational speed increases.

From another point of view, it seems that the material has witnessed a severe thermal cycle particularly when using the rotational speed of 837r.p.m as shown in Figure (28*a'*,*b'*,*c'*,*d'*,*e'*) whereas the severity manifests in the intensive rise of the workpiece temperature. Accordingly, the temperature in some parts of the workpiece

has exceeded the material solidus temperature. For this reason, it was possible to monitor the development in the time dependent liquid fraction over the thermal cycle. Thus, Figure (28*a*,*b*,*c*,*d*,*e*) presents several contours that exhibit how the liquid fraction in the material being welded would be affected due to the change in the material temperature. Because of the elevated heating rate, it can be seen from the figure that the material melting point was reached in the earlier stage of the thermal cycle as the maximum temperature that was registered at the moment of 3sec is around 852K. However, until three seconds no liquid has formed as presented in *a* and *b*. After 5sec, the maximum temperature was 929K which means that the melting temperature was already scored in some parts from the workpiece and accordingly the material converts to liquid state in those parts. In *c*,*d* and *e*, no magnification was needed as it can be seen that the tool is completely surrounded by the mushy zone in which the value of liquid fraction is ranging from the minimum of 0% at the outer face of the mushy zone to the maximum of 100% at the immediate vicinity of the tool. Additionally, the part of the mushy zone that has a high level of liquid fraction has noticeably expanded with the increase in the temperature. After a while, no more expanding will be there as it can be seen when comparing the scale of liquid fraction in *d* and *e*. The values of liquid fraction indicate that a relatively high amount of the welded material has converted to liquid which might cause defects in the welded joint. Figure (29) illustrates that the peak temperature is highly sensitive to the rotational speed which recorded 509K at speed of 237rpm while it was 975K for 837rpm.

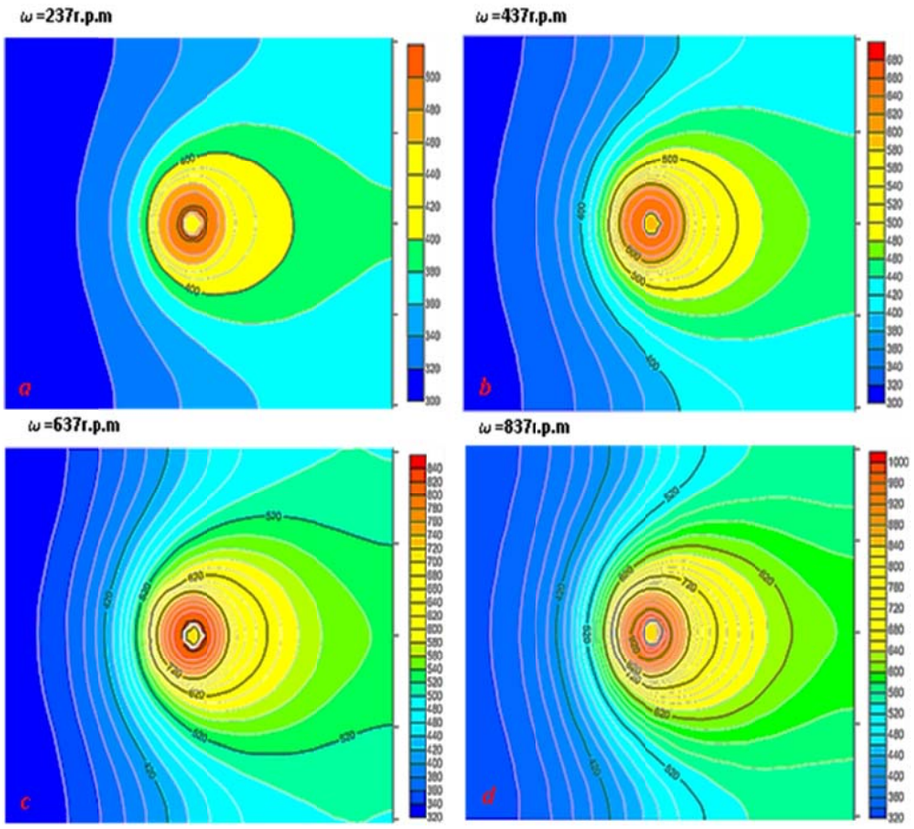

Figure 27: Static temperature contours for different rotational speeds

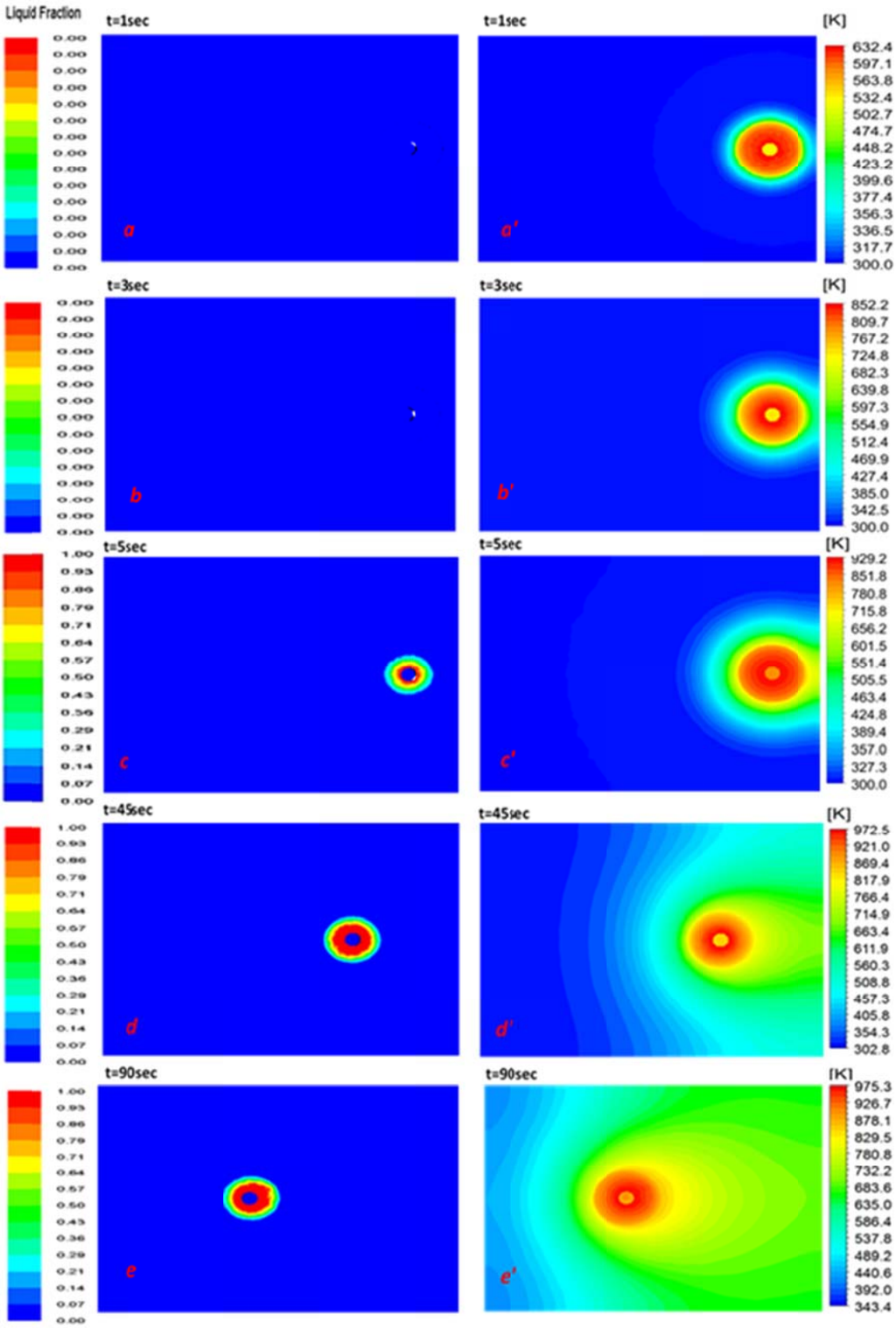

Figure 28: Liquid fraction contours corresponding to the temperature rising at different times for ω =837rpm

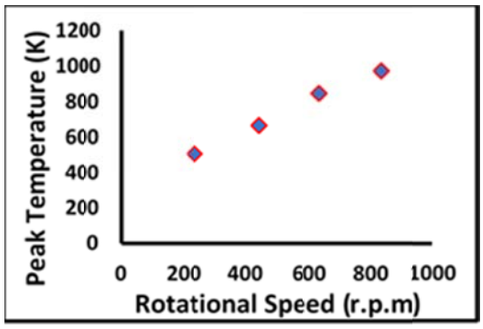

Figure 29: Peak temperature for different rotational speeds

Effects of the Axial Load

In Figure (30*a,b,c,d*), it can be seen how the temperature distribution around the tool change with the increase in the axial load where the general trend was similar to that observed when the tool rotational speed is changed. Additionally, the temperature has exceeded the material's solidus temperature for axial load of 14.2 MPa and then the liquid region is expected to appear**.**

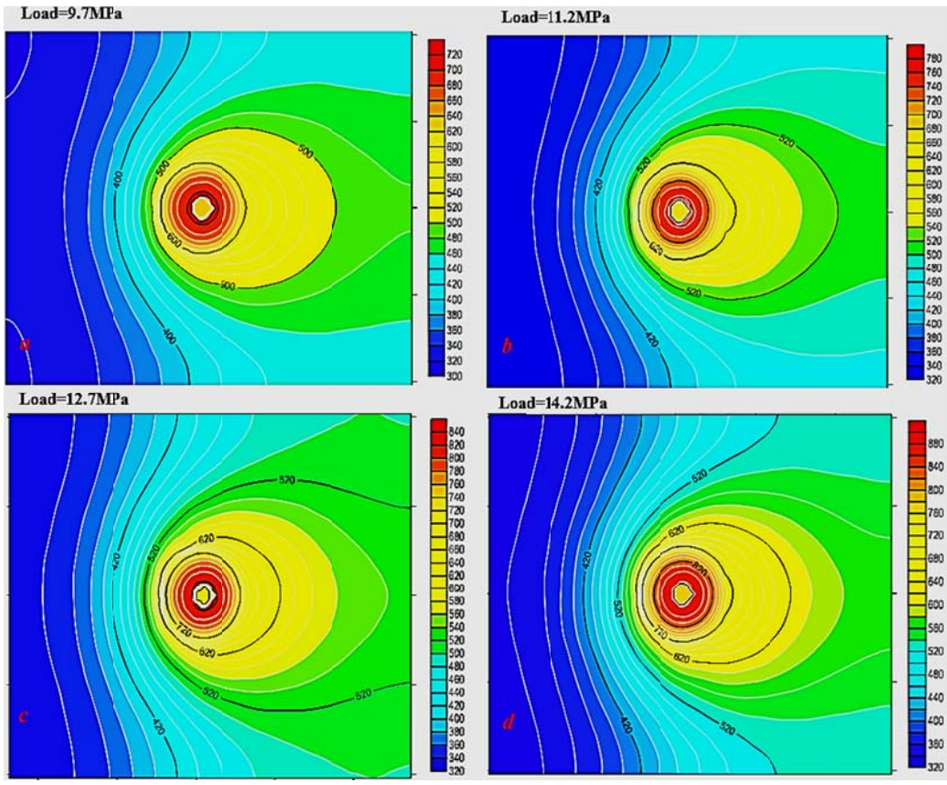

Figure 30: Static temperature contours for different axial loads

In Figure (31) snapshots of liquid fraction at different moments from the thermal cycle were taken to show the transient progression against the change in the temperature when the axial load is14.2MPa. By keeping in mind that the solidus temperature for the material used is 855K, it can be noticed from the figure that no melting has occurred in the first three seconds even though the average heating rate in this period reached to 96K/sec.

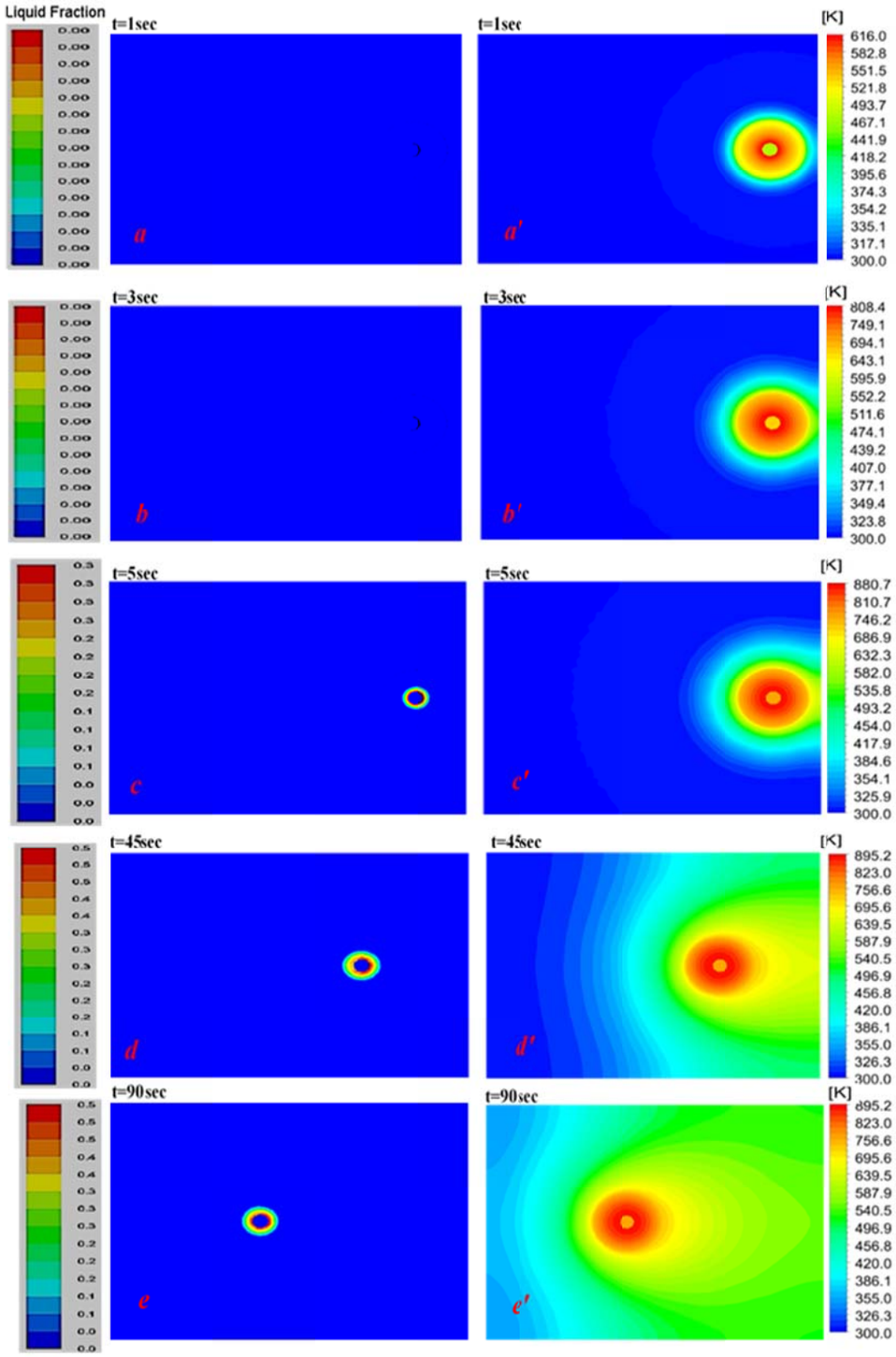

Figure 31: Liquid fraction contours corresponding to the temperature rising at different times for axial load = 14.2MPa

However, at t=5sec the model predicted a mushy zone with maximum liquid fraction of 30% as the instantaneous maximum temperature attained 881K. After a

period of the process time, the dimensions of mushy zone expanded whereas the maximum liquid fraction scored 50% at the moment of 45 seconds at which the temperature was around 895K. After 90seconds, the mushy zone stabilised, and no change has been recorded on the liquid fraction value compared to its value at the time of 45seconds. It can be seen in Figure (32) that the peak temperatures increase when the axial load increases. This can be justified by the increase in the frictional forces and the better frictional coupling which lead to boosting the heat generation in the interface between the tool and the workpiece [54].

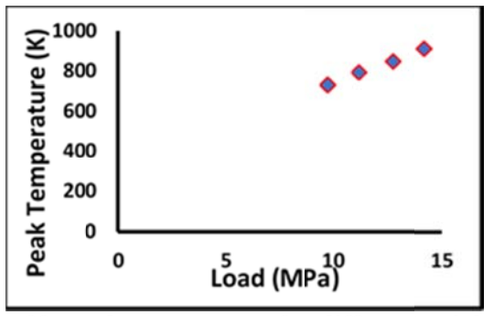

Figure 32: peak temperature for different axial loads

PREDICTION MODEL OF THE PEAK TEMPERATURE

As planned, the last step in this study is developing a prediction model for the peak temperature $\boldsymbol{T}_p$ that can be attained during FSW process. According to the literature review and based on the results which were previously presented and discussed, both the geometrical and operational parameters that have been considered in the thermal investigation showed an impact on the peak temperature. As a function of these parameters, a novel semi-empirical correlation for predicting the peak temperature can be developed based on the acquired data from CFD experiments and with the aid of an advanced statistical process which is multiple variable regression analysis. Therefore, the dimensionless equation (16) has been established to describe the relationship between the temperature ratio T_p / (T_s) and the considered variables.

$$\frac{\boldsymbol{T_p}}{\boldsymbol{T_s}} = \frac{\mathbf{0.01725}\ \left(\frac{H}{t}\right)^{0.091}\ \left(\frac{P}{P_{max}}\right)^{0.5469}}{\left(\frac{V}{\omega R_S}\right)^{0.6022}\ \left(\frac{n}{R_S}*\boldsymbol{R_P}\right)^{0.1165}} \tag{16}$$

where T_s is the solidus temperature of the material to be welded which is equal to 855K in the current study, V is the tool transverse speed, ω is the tool rotational speed, R_S is the shoulder radius, n is the number of pin side faces, H is the pin height, t is the workpiece thickness, P is the axial load, P_{max} is the maximum axial load used. Then, equation (16) can be rearranged to find a direct expression calculating $\boldsymbol{T}_p$ as following:

$$\boldsymbol{T_p} = \left[\frac{\mathbf{0.01725}\ \left(\frac{H}{t}\right)^{0.091}\ \left(\frac{P}{P_{max}}\right)^{0.5469}}{\left(\frac{V}{\omega R_S}\right)^{0.6022}\ \left(\frac{n}{R_S}*\boldsymbol{R_P}\right)^{0.1165}}\right] \times \boldsymbol{T_s} \tag{17}$$

It can be seen from the prediction model that (P/Pmax), (v/ωRs) have the most significant effect on the peak temperature. Moreover, the peak temperature is proportional to (H/t , P/P_{max}) and inversely proportional to (v/ωRs , N.Rp /Rs). From equation (17), if the fraction in the brackets has a value greater than 1, this means that some parts of the welded material converted to liquid state. In order to authorise the usefulness of equation (17), the average of difference between the values of $\boldsymbol{T}_p$

calculated from equation (17) and T_p values obtained from CFD was estimated to be 5.35%. Furthermore, it is obvious in Figure (33) that within errors ranged from 0 to maximum ±10%, it would be seen that around 90% of the data lies in this range. Thus, it can be concluded that the prediction model represents the peak temperature with reasonable accuracy. Last but not least, the above expressed equation is valid for the considered ranges of parameters.

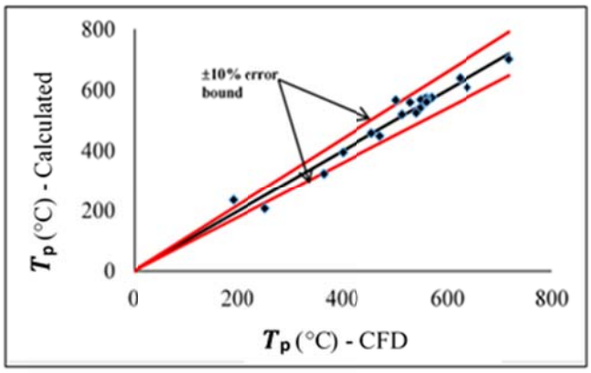

Figure 33: Prediction model of the peak temperature

CONCLUSIONS

A three – dimensional transient CFD model has been improved offering a more realistic representation to the physical model of friction stir welding. The adopted new modeling techniques have shown capability in avoiding the unnecessary assumptions. i.e. the dynamic mesh method that used to specify the translational movement of the welding tool has also helped to simulate a process with computation time reaching to 100sec. Moreover, considering the solidification and melting model has also led to minimise the fluid region which is an approximation and detecting the time-dependent values of liquid fraction. A reasonable accuracy was achieved from the improved CFD model as it has shown good agreement with the experimental measurements. From the analytical derivations carried out in this study regarding the heat generated in FSW when using polygonal pins, different mathematical expressions have been developed corresponding to the number of the pin faces. These novel equations are of extreme importance for a completion of the CFD simulation of FSW which aid to calculate the process heat input. The current CFD model captured the temporal and spatial temperature distribution throughout the weldments during the welding process for a wide range of variation in the geometrical and operational parameters. Noticably, for thick aluminium plates the temperature distribution is not mostly impacted by the increased heat value corresponding to the increase in the number of polygon side faces from 7 to 9. Furthermore, the increase in the welding parameters such as shoulder diameter, rotational speed and the axial force has obviously caused an increase in the temperatures while a marginal increase in the temperature recorded due to the increase in the pin height. Conversely, the increase in the workpiece thickness decreases the temperatures. A relative drop in the temperature caused by the increase in the pin diameter is noticed as well, however, an elevation in the temperature values can be observed when the heat generation from the tool pin can compensate that lost due to the accompanying decrease in the shoulder size. Based on the acquired numerical data from FSW processes using tools with polygonal pins, a semi-empirical relationship has been developed for the peak temperature within the workpiece. Finally, the results and the

analysis presented in this study would be of great value for the people who work in the welding field as the prediction model developed for the peak temperature can be used in where the welding procedure specifications are of interest.

ACKNOWLEDGEMENTS

This research was supported by the Libyan ministry of higher education and scientific research. All support is gratefully acknowledged.

NOMENCLATURE

V Tool Translational speed (m/sec)	n Number of Pin Side Faces
F Downward Force (N)	$Q^{\cdot}$ Activation Energy (kJ/mol)
P Contact (Axial) Pressure (Pa)	R Universal Gas Constant (J/mol. K)
Q Heat generated amount (W)	$c\,p$ Specific Heat (J/kg. K)
k Thermal Conductivity (W/(m.K))	x_1 TMAZ Design Variable (m)
T Temperature (K)	x_2 TMAZ Design Variable (m)
Ta The ambient Temperature (K)	Rs Shoulder Radius (m)
h Convective Heat Transfer Coefficient (W/m^2 .K)	Rp Pin Radius (m)
Z The Zener-Hollomon Parameter	H Pin Height (m)
$A^{\cdot}$ Material Constant (1/sec)	
C Courant number	

GREEK SYMBOLS

ω Tool Rotational Speed (r.p.m)	σ_E The effective stress (Pa)
β Liquid Fraction	α Material Constant (MPa^{-1})
$\tau_{contact}$ Contact Shear Stress (Pa)	$\varepsilon^{\cdot}$ Strain Rate
$\tau_{friction}$ Frictional Shear Stress (Pa)	η The fluid Viscosity (Pa. sec)
μ Friction Coefficient	ρ Material Density (kg/m^3)
ε The Stefan-Boltzmann Constant (W/m^2·K^4)	π Pi

REFERENCES

[1] Gibson, B. T., Lammlein, D. H., Prater, T. J., Longhurst, W. R., Cox, C. D., Ballun, M. C., and Strauss, A. M. (2014). Friction stir welding: Process, automation, and control. *Journal of Manufacturing Processes*, 16(1), 56-73.

[2] Mishra, R.S., P.S. De, and N. Kumar, Friction Stir Welding and Processing. *Science and Engineering*. 2014, Dordrecht: Springer International Publishing.

[3] Schmidt, H., Hattel, J., & Wert, J. (2003). An analytical model for the heat generation in friction stir welding. *Modelling and simulation in materials science and engineering*, 12(1), 143.

[4] Mehta, M., Reddy, G. M., Rao, A. V., & De, A. (2015). Numerical modeling of friction stir welding using the tools with polygonal pins. *Defence Technology*, 11(3), 229-236.
[5] Mehta, M., De, A., & DebRoy, T. (2014). Material adhesion and stresses on friction stir welding tool pins. *Science and Technology of Welding and Joining*, 19(6), 534-540.
[6] Darmadi, D. B., & Talice, M. (2020). Improving the strength of friction stir welded joint by double side friction welding and varying pin geometry. *Engineering Science and Technology, an International Journal*. 24(3), 637-647
[7] Fujii, H., Cui, L., Maeda, M., & Nogi, K. (2006). Effect of tool shape on mechanical properties and microstructure of friction stir welded aluminum alloys. *Materials Science and Engineering: A*, 419(1-2), 25-31.
[8] Elangovan, K., & Balasubramanian, V. (2007). Influences of pin profile and rotational speed of the tool on the formation of friction stir processing zone in AA2219 aluminium alloy. *Materials Science and Engineering: A*, 459(1-2), 7-18.
[9] Elangovan, K., Balasubramanian, V., & Valliappan, M. (2008). Influences of tool pin profile and axial force on the formation of friction stir processing zone in AA6061 aluminium alloy. *The international journal of advanced manufacturing technology*, 38(3-4), 285-295.
[10] Elangovan, K., & Balasubramanian, V. (2008). Influences of tool pin profile and tool shoulder diameter on the formation of friction stir processing zone in AA6061 aluminium alloy. *Materials & design*, 29(2), 362-373
[11] Gharaibeh, N., Al-Jarrah, J. A., & Sawalha, S. A. (2016). Effect of pin profile on mechanical properties of 6061 al alloy welded joints prepared by friction stir welding. *Triangle*, 11(96.16), 1-42..
[12] Biswas, P., A Kumar, D., & Mandal, N. R. (2012). Friction stir welding of aluminum alloy with varying tool geometry and process parameters. Proceedings of the Institution of Mechanical Engineers, Part B: *Journal of Engineering Manufacture, 226(4), 641-648.*
[13] Vijay, S. J., & Murugan, N. (2010). Influence of tool pin profile on the metallurgical and mechanical properties of friction stir welded Al–10 wt.% TiB2 metal matrix composite. *Materials & Design*, 31(7), 3585-3589.
[14] Gopalakrishnan, S., & Murugan, N. (2011). Prediction of tensile strength of friction stir welded aluminium matrix TiCp particulate reinforced composite. *Materials & Design*, 32(1), 462-467.
[15] Palanivel, R., Mathews, P. K., Murugan, N., & Dinaharan, I. (2012). Effect of tool rotational speed and pin profile on microstructure and tensile strength of dissimilar friction stir welded AA5083-H111 and AA6351-T6 aluminum alloys. *Materials & Design*, 40, 7-16.
[16] Vijayan, D., & Rao, V. S. (2014). A Multi Response Optimization of Tool Pin Profile on the Tensile Behavior of Age-hardenable Aluminum Alloys during Friction Stir Welding. *Research Journal of Applied Sciences, Engineering and Technology*, 7(21), 4503-4518.
[17] Patel, V. V., Badheka, V., & Kumar, A. (2017). Effect of polygonal pin profiles on friction stir processed superplasticity of AA7075 alloy. *Journal of materials processing technology*, 240, 68-76.

[18] Mugada, K. K., & Adepu, K. (2019). Effect of knurling shoulder design with polygonal pins on material flow and mechanical properties during friction stir welding of Al–Mg–Si alloy. *Transactions of Nonferrous Metals Society of China*, 29(11), 2281-2289.
[19] Buffa, G., Hua, J., Shivpuri, R., & Fratini, L. (2006). Design of the friction stir welding tool using the continuum based FEM model. *Materials Science and Engineering*: A, 419(1-2), 381-388.
[20] Patel, J. B., & Patil, H. S. (2014). Simulation of peak temperature & flow stress during FSW of aluminium alloy AA6061 for various tool pin profiles. *Int J Mater Sci Eng*, 2(1), 67-71.
[21] Marzbanrad, J., Akbari, M., Asadi, P., & Safaee, S. (2014). Characterization of the influence of tool pin profile on microstructural and mechanical properties of friction stir welding. *Metallurgical and Materials Transactions B*, 45(5), 1887-1894.
[22] Su, H., Wu, C. S., Bachmann, M., & Rethmeier, M. (2015). Numerical modeling for the effect of pin profiles on thermal and material flow characteristics in friction stir welding. *Materials & Design*, 77, 114-125.
[23] Ulysse, P. (2002). Three-dimensional modeling of the friction stir-welding process. *International Journal of Machine Tools and Manufacture*, 42(14), 1549-1557.
[24] Colegrove, P. A., & Shercliff, H. R. (2005). 3-Dimensional CFD modelling of flow round a threaded friction stir welding tool profile. *Journal of materials processing technology*, 169(2), 320-327.
[25] Crawford, R., Cook, G. E., Strauss, A. M., & Hartman, D. A. (2006). Modelling of friction stir welding for robotic implementation. *International Journal of Modelling, Identification and Control*, 1(2), 101-106.
[26] Nandan, R., Roy, G. G., Lienert, T. J., & DebRoy, T. (2006). *Numerical modelling of 3D plastic flow and heat transfer during friction stir welding of stainless steel*. Science and Technology of Welding and Joining, 11(5), 526-537.
[27] Atharifar, H., Lin, D., & Kovacevic, R. (2009). Numerical and experimental investigations on the loads carried by the tool during friction stir welding. *Journal of Materials Engineering and Performance*, 18(4), 339-350.
[28] Aljoaba, S. Z., Jawahir, I. S., Dillon, O. W., Ali, M. H., & Khraisheh, M. K. (2009). Modeling of friction stir processing using 3D CFD analysis. *International journal of material forming*, 2(1), 315-318.
[29] Lin, S. B., Zhao, Y. H., He, Z. Q., & Wu, L. (2011). Modeling of friction stir welding process for tools design. *Frontiers of Materials Science*, 5(2), 236-245.
[30] Yu, Z., Zhang, W., Choo, H., & Feng, Z. (2012). Transient heat and material flow modeling of friction stir processing of magnesium alloy using threaded tool. *Metallurgical and Materials Transactions A*, 43(2), 724-737.
[31] Mohanty, H., Mahapatra, M. M., Kumar, P., Biswas, P., & Mandal, N. R. (2012). Study on the effect of tool profiles on temperature distribution and material flow characteristics in friction stir welding. Proceedings of the Institution of Mechanical Engineers, Part B: *Journal of Engineering Manufacture*, 226(9), 1527-1535.

[32] WU, C. S., ZHANG, W. B., Lei, S. H. I., & CHEN, M. A. (2012). Visualization and simulation of plastic material flow in friction stir welding of 2024 aluminium alloy plates. *Transactions of Nonferrous Metals Society of China*, 22(6), 1445-1451.
[33] Chen, G. Q., Shi, Q. Y., Li, Y. J., Sun, Y. J., Dai, Q. L., Jia, J. Y., ... & Wu, J. J. (2013). Computational fluid dynamics studies on heat generation during friction stir welding of aluminum alloy. *Computational Materials Science*, 79, 540-546.
[34] Ji, S., Xing, J., Yue, Y., Ma, Y., Zhang, L., & Gao, S. (2013). Design of friction stir welding tool for avoiding root flaws. *Materials*, 6(12), 5870-5877.
[35] Cho, H. H., Hong, S. T., Roh, J. H., Choi, H. S., Kang, S. H., Steel, R. J., & Han, H. N. (2013). Three-dimensional numerical and experimental investigation on friction stir welding processes of ferritic stainless steel. *Acta Materialia*, 61(7), 2649-2661.
[36] Chen, G. Q., Shi, Q. Y., Fujiya, Y., & Horie, T. (2014). Simulation of metal flow during friction stir welding based on the model of interactive force between tool and material. *Journal of materials engineering and performance*, 23(4), 1321-1328.
[37] Kang, S. W., Jang, B. S., & Kim, J. W. (2014). A study on heat-flow analysis of friction stir welding on a rotation affected zone. *Journal of mechanical science and technology*, 28(9), 3873-3883.
[38] Zhang, Z., & Wu, Q. (2015). Analytical and numerical studies of fatigue stresses in friction stir welding. *The International Journal of Advanced Manufacturing Technology*, 78(9-12), 1371-1380.
[39] Kadian, A. K., & Biswas, P. (2015). A comparative study of material flow behavior in friction stir welding using laminar and turbulent models. *Journal of Materials Engineering and Performance*, 24(10), 4119-4127.
[40] Gadakh, V. S., Kumar, A., & Patil, G. V. (2015). Analytical modeling of the friction stir welding process using different pin profiles. *Welding Journal*, 94(4), 115-124.
[41] Hamza, E., Asim, T., & Mishra, R. (2016). Computational Fluid Dynamics based Transient Thermal Analysis of Friction Stir Welding. *6th International and 43rd National Conference on Fluid Mechanics and Fluid Power (FMFP-2016)*. December 2016: Allahabad, India
[42] Hamza, E. (2020). Dimensions Effect of the Rotating Fluid Zone on the Results when CFD Modeling of Friction Stir Welding. *Third Conference for Engineering Sciences and Technology (CEST-2020).* 01-03 December 2020 /Alkhoms - Libya
[43] Nandan, R., Roy, G. G., & Debroy, T. (2006). Numerical simulation of three-dimensional heat transfer and plastic flow during friction stir welding. *Metallurgical and materials transactions A*, 37(4), 1247-1259.
[44] FLUENT online manual. Available from: http://www.ansys.com/products/fluiddynamics/.
[45] Ansys 13.0.0 User Guide
[46] Mishra, R. S., & Ma, Z. Y. (2005). Friction stir welding and processing. *Materials science and engineering: R*: reports, 50(1-2), 1-78.

[47] Al-Abidi, A. A., Mat, S. B., Sopian, K., Sulaiman, M. Y., & Mohammed, A. T. (2013). CFD applications for latent heat thermal energy storage: a review. *Renewable and sustainable energy reviews*, 20, 353-363.
[48] Muhieddine, M., Canot, E., & March, R. (2009). Various approaches for solving problems in heat conduction with phase change. *International Journal on Finite* Volumes, 19.
[49] Gadakh, V. S., & Adepu, K. (2013). Heat generation model for taper cylindrical pin profile in FSW. *Journal of Materials Research and Technology*, 2(4), 370-375.
[50] Kang, S. W., & Jang, B. S. (2014). Comparison of friction stir welding heat transfer analysis methods and parametric study on unspecified input variables. *Journal of Mechanical Science and Technology,* 28(10), 4233-4246.
[51] Dudley, J. Selecting a Target Transient Time Step in a CFD Analysis. 2015 27 Mach; Available from: https://caeai.com/blog/selecting-target-transient-time-step-cfd-analysis.
[52] Radius of a regular polygon. Available from: http://www.mathopenref.com/polygonradius.html.
[53] Neto, D. M., & Neto, P. (2013). Numerical modeling of friction stir welding process: a literature review. *The International Journal of Advanced Manufacturing Technology*, *65*(1-4), 115-126.
[54] Welding, E. B., & Handbook, A. S. M. (1993). *Welding, brazing, and soldering*. ASM Int, 6, 254.
[55] Colegrove, P. A., Shercliff, H. R., & Zettler, R. (2007). Model for predicting heat generation and temperature in friction stir welding from the material properties. *Science and Technology of Welding and Joining*, 12(4), 284-297.